Application of in-silico and in-vitro optogenetic tools to cardiac arrhythmia research

Teplenin, A.

Chapter 2

"Trapped Reentry" as Source of Acute Focal Atrial Arrhythmias

Tim De Coster, PhD[*,1]; Alexander S. Teplenin, MSc[*,1]; Iolanda Feola, PhD[1]; Cindy I. Bart[1]; Arti A. Ramkisoensing, PhD[1]; Bram L. den Ouden[1]; Dirk L. Ypey, PhD[1]; Serge A. Trines, MD, PhD[1]; Alexander V. Panfilov, PhD[1,2,3,4]; Katja Zeppenfeld, MD, PhD[1]; Antoine A.F. de Vries, PhD[1]; Daniël A. Pijnappels, PhD[1]

[1]Laboratory of Experimental Cardiology, Department of Cardiology, Heart Lung Center Leiden, Leiden University Medical Center, Leiden, the Netherlands
[2]Department of Physics and Astronomy, Ghent University, Ghent, Belgium
[3]Ural Federal University, Ekaterinburg, Russia
[4]World-Class Research Center "Digital biodesign and personalized healthcare", Sechenov University, Moscow, Russia

[*] *equal contributions*

Cardiovascular Research (2023): cvad179

GRAPHICAL ABSTRACT

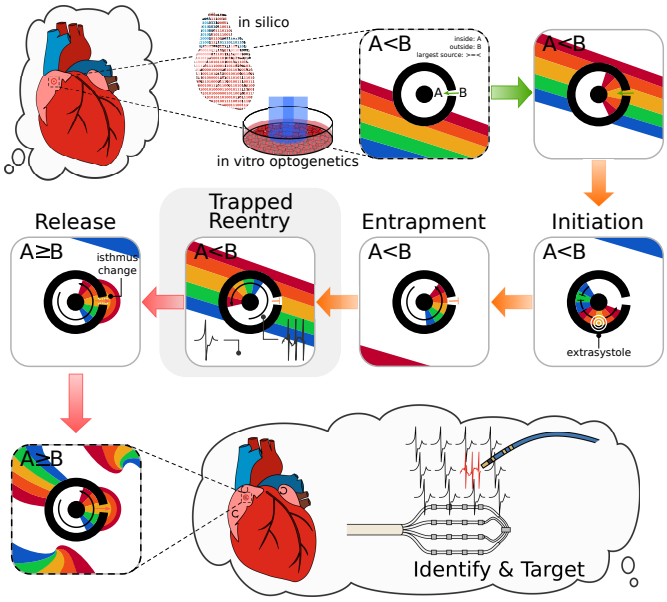

Abstract
AIMS: Diseased atria are characterized by functional and structural heterogeneities, adding to abnormal impulse generation and propagation. These heterogeneities are thought to lie at the origin of fractionated electrograms recorded during sinus rhythm (SR) in atrial fibrillation (AF) patients and are assumed to be involved in the onset and perpetuation (e.g. by reentry) of this disorder. The underlying mechanisms, however, remain incompletely understood. Here, we tested whether regions of dense fibrosis could create an electrically isolated conduction pathway (EICP) in which reentry could be established via ectopy and local block to become "trapped". We also investigated whether this could generate local fractionated electrograms and whether the reentrant wave could "escape" and cause a global tachyarrhythmia due to dynamic changes at a connecting isthmus.
METHODS AND RESULTS: To precisely control and explore the geometrical properties of EICPs, we used light-gated depolarizing ion channels and patterned illumination for creating specific non-conducting regions *in silico* and *in vitro*. Insight from these studies was used for complementary investigations in virtual human atria with localized fibrosis. We demonstrated that a reentrant tachyarrhythmia can exist locally within an EICP with SR prevailing in the surrounding tissue and identified conditions under which reentry could escape from the EICP, thereby converting a local latent arrhythmic source into an active driver with global impact on the heart. In a realistic 3-dimensional model of human atria, unipolar epicardial pseudo-electrograms showed fractionation at the site of "trapped reentry" in coexistence with regular SR electrograms elsewhere in the atria. Upon escape of the reentrant wave, acute arrhythmia onset was observed.
CONCLUSIONS: Trapped reentry as a latent source of arrhythmogenesis can explain the sudden onset of focal arrhythmias, which are able to transgress into AF. Our study might help to improve the effectiveness of ablation of aberrant cardiac electrical signals in clinical practice.
TRANSLATIONAL PERSPECTIVE: Abnormal electrical behavior under sinus rhythm has been found in the atria in the form of so-called complex fractionated atrial electrograms and AF-nests. We show that this behavior could be a sign of an underlying sleeping arrhythmia, here referred to as trapped reentry, that can wake up and render the whole atria into global arrhythmia. With this new insight we aim to trigger the active search for trapped reentry circuits in patients, to incite discussion among cardiac electrophysiologists about the clinical relevance of (awaking) dormant arrhythmias, and to fuel the search for improvements in arrhythmia treatment.

1 Introduction

IRREGULAR beating in the two upper chambers of the heart, such as during atrial fibrillation (AF), is associated with increased cardiovascular morbid-

ity, mortality, and impaired quality of life[1]. To improve AF-related therapeutic strategies, it is important to enlarge insight in the electrophysiological mechanisms underlying this cardiac arrhythmia. Diseased atria are characterized by structural heterogeneities (e.g. fibrotic regions) and functional heterogeneities (e.g. areas of altered conduction not associated with an anatomical obstacle). Such areas of altered texture and conduction are revealed by abnormal electrograms or complex fractionated atrial electrograms (CFAEs)[2]. The regions in which these CFAEs occur often display an increased collagen content ([micro]fibrosis) and myocardial fiber dissociation[3]. The spatial distribution of these structural changes rather than the amount of collagen is the major determinant of the occurrence and appearance of CFAEs[4]. Pathological distributions of structural or functional heterogeneities produce differences in electrical load in the conduction pathway, creating 'non-uniform anisotropic' impulse propagation[5]. They add to abnormal impulse generation and propagation, originating from e.g. ectopy[6] and unidirectional conduction block[7], creating various sources of reentrant activity, which lead to arrhythmias including AF. These arrhythmogenic conduction events can occur in very small areas (e.g. reentrant circuits as small as 0.6×2.6 mm) in human atrial bundles[8,9]. AF can be sustained by localized sources in the form of electrical rotors and focal impulses, for which catheter ablation improves clinical outcome[10–12]. It might be speculated that these patient-specific sources correlate with areas of atrial fibrosis in which the site-specific micro-architecture of connective tissue fibers and the remaining myocardial fibers allow reentrant activity to occur and to sustain[8]. The elimination of CFAEs by single ablation lesions[13], which typically have a diameter of 5 to 7 mm, is in accordance with the possibility that very small reentrant circuits underlie CFAEs. CFAEs have been selected as targets to treat AF[10,14], leading up to as high as a 91% one-year success rate. Although it has been suggested that these electrograms may represent areas of slow conduction or pivoting points in circuits of reentry associated with AF, the mechanism underlying the various types of CFAEs has not been fully elucidated[15]. One of these cases of which the origin is not clear, was the detection of CFAEs during sinus rhythm (SR)[16]. Here, we provide an explanation for such CFAE observations which might lead to sudden arrhythmia initiation. This explanation merges micro-reentry and source-sink mismatch. Using computer simulations and monolayers of optogenetically modified (i.e. Ca^{2+}-translocating channelrhodopsin [CatCh]-expressing[17]) neonatal rat atrial myocytes (NRAMs)[18] to create structural heterogeneities, we show that a source of reentrant excitation can be electrically shielded from the remaining part of the atria. The electrical separation of the source of reentrant excitation can occur due to current-to-load mismatch[19] between the shielded region and the remaining atrial tissue. When this source is electrically shielded, it will coexist with normal heart beats and thus induce CFAEs during SR. However, some factors, e.g. partial cellular uncoupling[20] can reduce that current-to-load mismatch and the initially isolated reentrant wave will start to affect the rest of the atria causing an atrial

arrhythmia. Due to the fact that the reentrant source can lock itself away from the rest of the atrial tissue, we have coined it "trapped reentry".

2 METHODS

Expanded Methods can be found in the Supplemental Material (sections 1.1-4.7) and Major Resources Table.

2.1 Data Availability

The data that support the findings of this study are available from the corresponding author upon reasonable request.

2.2 Experimental Methods

All animal experiments were reviewed and approved by the Animal Experiments Committee of the Leiden University Medical Center (AVD116002017818 and AVD15460) and performed in accordance with the recommendations for animal experiments issued by the European Commission directive 2010\63.

Preparation of neonatal rat atrial monolayers

Two-day-old Wistar rats (RRID:RGD_737929) were sedated with the use of isoflurane (2-3%) inhalation, after which the animals were decapitated and direct brain activity was inactivated through liquid nitrogen. Subsequently the hearts were excised and cells from the atrial tissue of these hearts were isolated and plated to form NRAM monolayers.

Optical Voltage Mapping of Monolayers of CatCh-expressing NRAMs

Monolayers of NRAMs (from 2-day-old Wistar rats) were genetically modified with a lentiviral vector encoding the depolarizing light-gated ion channel CatCh resulting in homogeneous transduction of nearly 100% of the cells[21]. Only monolayers showing uniform action potential propagation upon 1-Hz electrical pacing were further used (n=13). Optical voltage mapping was performed with a MiCAM05-Ultima camera (SciMedia, Costa Mesa, CA), measuring at 167 Hz frame rate a 100 x 100 pixel image covering an area of either 1.65 x 1.65 cm^2 (n=8) or 1.01 x 1.01 cm^2 (n=5). The resulting images were used to investigate entrapment and escape of excitation waves in these CatCh-expressing monolayers by using a patterned illuminator connected to a 470-nm LED source[18], resulting in blue light at cell level with an intensity of 30 mW/cm^2.

Optical Pattern Design

For the NRAM monolayers, the circuit of trapped reentry was created between two separate non-conducting circular regions in wells of 24-well cell culture plates. The inner circle had a diameter of 0.26 cm; the inside and outside diameter of the surrounding ring were 0.65and 0.93 cm, respectively. The dimensions of the horizontal light-bands were 1.467 × 0.187 cm^2 (height × width), with funnel openings of varying width ranging from 0.244 cm down to 0.041 cm.

Stimulation Protocol

A trapped wave was created inside the optogenetically constructed region of isolated conduction by programmed optical stimulation (S1S2 protocol, Figure S1). During this process, periodic electrical stimulation was applied from the bottom left of the culture, mimicking SR in the atria. These pulses were delivered at a frequency of 1-Hz through an epoxy-coated bipolar platinum electrode delivering square 10-ms, 8-V suprathreshold electrical impulses via a STG 2004 stimulus generator and MC Stimulus II software (both from Multi Channel Systems, Reutlingen, Germany) and were continuously applied.

2.3 Computational Methods

The transmembrane voltage (V) was calculated in millivolts (mV), evolving spatiotemporally and obeying the reaction-diffusion equation:

$$\frac{\partial V}{\partial t} = \nabla(D\nabla V) - (I_{ion} + I_{stim})/C_m \tag{1}$$

where t is time in milliseconds (ms), I_{ion} is the total ionic current density in microampere per square centimeter ($\mu A/cm^2$), I_{stim} is the external stimulus current in $\mu A/cm^2$, C_m is the specific membrane capacitance in microfarad per square centimeter ($\mu F/cm^2$), and D is the conduction tensor, which determines the electrical conductivity of cardiac tissue in each direction of propagation, i.e. the mathematical representative of gap junctional coupling efficiency.

Simulations of NRAM Monolayers

The electrophysiological properties of NRAMs in a homogenous monolayer were modelled according to *Majumder et al.*[22]. The optogenetic tool used in the numerical studies was a previously described model of *Chlamydomonas reinhardtii* channelrhodopsin-2 mutant H134R[23]. In order to demonstrate the trapping of a reentrant wave, we designed several "illumination" patterns that were projected onto our in silico monolayers. From the center to the center to the periphery consisted of an illuminated circle, a ring of unexposed tissue and

a ring of illuminated tissue with strategically positioned funnels (isthmi) of the desired opening angles.

Simulations of Human Atria

For human atrial tissue simulations, anatomical data and fiber directions were obtained from Dössel et. al[24] for realistic anisotropic simulations. The three ionic cell models that were used are the Courtemanche model[25], the AF-induced electrically remodeled human atrial Courtemanche model[26], and the chronic AF-remodeled human atrial Loewe model[27] (Figure S2).

Funnel Opening Design

Both in the 2-dimensional (2D) and 3-dimensional (3D) models, the design of the funnel-shaped connection between the circuit of trapped reentry and the surrounding cardiac tissue was based on the underlying principles of source-sink mismatch. To create the conditions leading to unidirectional conduction block, the end of the funnel touching the bulk of the tissue was provided with a smaller surface area than the end touching the inner circuit.

Circuit Design

For the *in silico* NRAM monolayers, the circuit had identical dimensions to the one *in vitro*. The 3D *in silico* human atria were bounded by a box with dimensions of $10.755 \times 8.895 \times 7.035$ cm^3, which corresponds to the size of the atria of human adults[28]. For the region of trapped reentry, the size of the inner obstacle was 1.410 × 0.468 cm2 × local wall thickness and that of the circuit (i.e. inner obstacle plus conducting region) was 2.694×1.8375 cm^2 × local wall thickness.

Stimulation Protocols

For *in silico* 2D monolayers of NRAMs, an S1S2 protocol was used to induce trapped reentry. Once trapped reentry was established, either no or 1 Hz bulk pacing was performed. All *in silico* 3D human atrial models were pre-paced 50 times at 1 Hz at the single cell level to start with stable cell parameters, after which they were used for whole atria simulations. To establish trapped reentry, again an S1S2 protocol was used. For the S1 pulse, the sinus node was activated in the atria. The S2 pulse was timed inside the circuit of trapped reentry. Once trapped reentry was established, pacing continued from the sinus node at 1 Hz. Each simulation lasted 12 seconds.

Electrogram Computation

The extracellular potential ϕ_e (for unipolar electrograms) was modelled using a current source approximation for a large volume conductor:

$$\phi_e(x,t) = \frac{1}{4\pi\sigma_e}\int_a^b d\mathbf{y}\,\frac{I_m(y,t,)}{|\mathbf{x}-\mathbf{y}|} \tag{2}$$

where **x** is the electrode location vector, **y** is the current source location vector, I_m is the transmembrane current per unit area of atrial tissue surface, and $\sigma_e = 5.34 mS/cm$ is the extracellular conductivity[29].

3 RESULTS

We demonstrate the principle of trapped reentry by reproducing its three distinct and subsequent phases: (1) SR, (2) a trapped excitation wave not affecting SR in the surrounding tissue, and (3) the phase in which the reentrant waves are transmitted to the surrounding tissue. We show this principle in a simplified, fully controllable 2D in silico model of NRAMs, in an experimental in vitro model of optogenetically modified monolayers of NRAMs, and, lastly, in a realistic 3D model, i.e. an in silico digital twin of whole human atria containing a fibrotic area capable of accommodating a reentrant wave.

3.1 Trapped Reentry in a 2D *In Silico* Model of NRAMs

The principle of trapped reentry was first demonstrated in a simplified controllable system (that could later be realized experimentally): an *in silico* monolayer model of NRAMs[22] (Figure 1, Video V1). Excitation and conduction block were mimicked by the introduction of a virtual channelrhodopsin into the cells[23]. When these light-gated cation channels are activated by simulated light, a depolarizing current is generated that keeps the membrane potential elevated as long as the light is on, rendering the illuminated regions inexcitable. Consequently, any geometry of structural heterogeneity can be created, e.g. a defined geometry of depolarized tissue containing an isolated conductive circuit, with an isthmus to access it from the outside. The simplest construction of such a geometry is shown in Figure 1A and 1B: an isolated circuit between two circular obstacles with an isthmus in the outer ring. Establishment of trapped reentry in this isolated circuit involved the following steps:

1. Patterned light pulse to create the circuit of trapped reentry (Figure 1A1),
2. S1 pulse inside the circuit to initiate excitation waves propagating in both directions (Figure 1A2),
3. Properly timed S2 pulse, simulating an ectopic pulse, to block counterclockwise wave propagation and initiate reentry (Figure 1A3),

4. Consolidation of trapped reentry due to current-to-load mismatch at the isthmus (Figure 1A4).

Escape of the trapped waves is shown in Figure 1B. While it can be achieved by various means (Figure 1C3), in our case we globally modified sodium channel and gap junctional conductance (G_{Na} and G_{gap}, respectively). Decreasing the

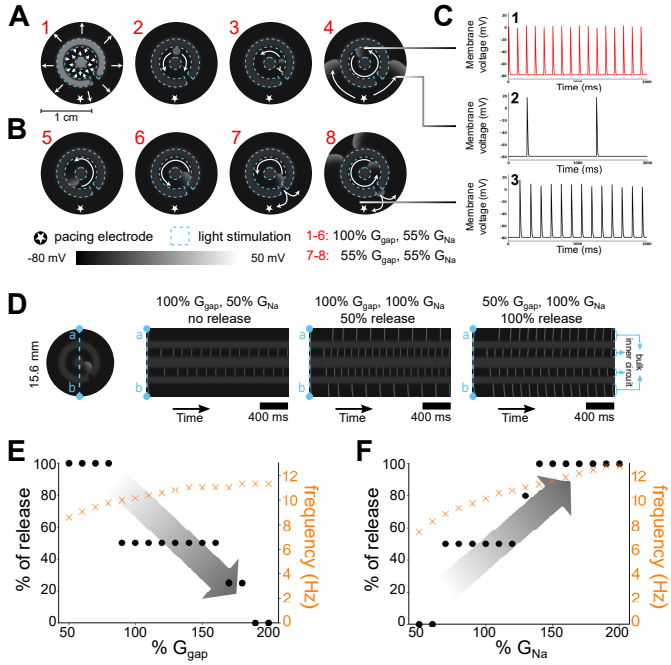

Figure 1 – **In silico realization of trapped reentry (2D model).** A, Procedure to initiate a trapped reentrant wave. Blue lines demarcate the inner circle and outer ring in which the channelrhodopsin channels are activated. White areas are depolarized, black areas are repolarized. B, Escape of a reentrant trapped wave following reduction of gap junctional coupling. C, Voltage traces of three selected representative points showing trapped reentry with SR in the surrounding bulk tissue in A4 and escape of the reentrant wave through an isthmus in B8. D, Line analysis of the electrical activity through the center of the circuit (vertical axis) over time (horizontal axis). Different release rhythms are observed depending on the global parameters used in the model (see the signals in the bulk tissue at the top and bottoms of each panel). Scale bar: 400 ms. E, Escape and rotational frequency of trapped waves at different levels of gap junctional coupling (G_{Na}=100%). F, Escape and rotational frequency of trapped waves at different sodium conductances (G_{gap}=100%).

sodium conductance increases source-sink (reentry circuit-surrounding tissue bulk) mismatch from inside to outside at the isthmus, and therefore promoted excitation wave trapping. On the other hand, decreasing gap junctional coupling decreases source-sink mismatch, helping the reentrant waves to escape (Figure 1B). Different release patterns were found by adjusting these two parameters, going from total block to release of every reentrant wave that passed

the isthmus. Figure 1D shows a narrow slice of the 2D tissue through the center of the circuit (vertical axis) over time (horizontal axis) in which three different situations are depicted, i.e. no release or block (50% G_{Na}, 100% G_{gap}), 50% release (100% G_{Na}, 100% G_{gap}), and 100% release (100% GNa, 50% G_{gap}). To get more insight into the process of trapping and releasing a reentrant wave, each of the two parameters was varied separately while the other one was kept constant at 100% (Figure 1E and 1F, Video V1). The capture rate, expressed as the percentage of waves that is able to escape, depended on the extent of source-sink mismatch. While a decrease in sodium conductance impeded isthmus conduction, a decrease in the gap junctional coupling promoted it. This shows that it is possible to control trapped reentry by means of changing just two global parameters.

3.2 Trapped Reentry in a 2D *In Vitro* Model of NRAMs

Monolayers of CatCh-expressing NRAMs were subjected to patterned illumination to establish conditions for trapped reentry in a cell culture model (Figure 2, Video V2 and V3).

After establishing the geometrical circuit (Figure 2A1), a trapped wave was created inside the optogenetically constructed region of isolated conduction just like *in silico* by means of an S1S2 protocol (S1: Figure 2A2; S2: Figure 2A3). This resulted in trapping of a reentrant wave (Figure 2A4) with a frequency between 7.58 and 13.89 Hz inside the isolated region and SR of 1 Hz in the remainder of the monolayer.

Patterned illumination provides an easy possibility to directly influence the source-sink mismatch at the isthmus with the required level of precise control. By projecting patterns with a variety of isthmus widths, control over entrapment and escape of reentrant waves could be exerted (Figure 2B), which revealed more frequent escapes of reentrant waves under wider isthmi. For all 8 out of 8 NRAM monolayers it was possible to create trapped reentry with this protocol.

Entrapment and escape of a reentrant wave was demonstrated by representative optical voltage traces out of one NRAM monolayer showing a trapped wave in the reentry circuit (Figure 2C1), SR in the surrounding tissue bulk (Figure 2C2) and a focal arrhythmia in the bulk tissue originating from the reentry circuit (Figure 2C3). The fact that the top and bottom trace have the same frequency, indicates that the outer area was paced by the excitation waves that escaped from the reentry circuit and no longer by sinus pulses. The reentrant drivers had a frequency of 10.41 ± 2.65 Hz (Figure 2D). Conduction velocities under a regular sinus pulse (15.40 ± 1.99 cm/s) through the monolayer were comparable to those inside (14.43 ± 2.91 cm/s) and outside (16.46 ± 2.78 cm/s) the reentry circuit (Figure 2E-F), showing little optogenetic effects on cardiac conduction velocities.

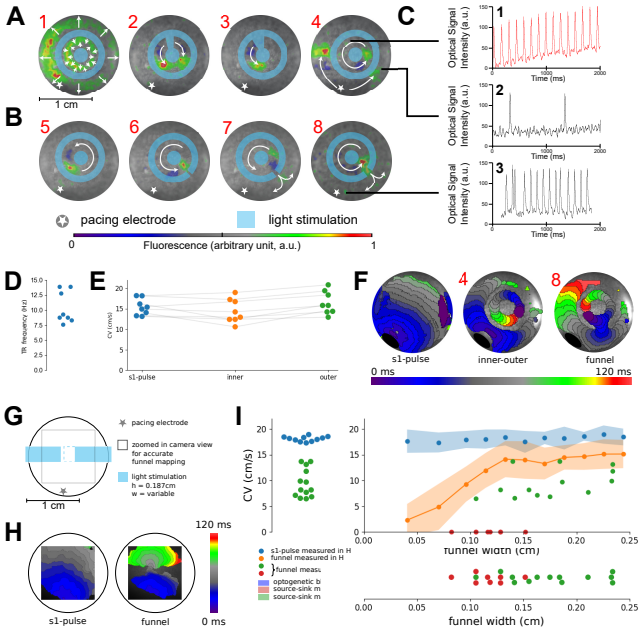

Figure 2 – **In vitro realization of trapped reentry (2D model).**Procedure to initiate a trapped reentrant wave (repeated for n=8 biological/technical replicates) . The light blue color shows the illumination pattern used to locally inactivate the tissue. White arrows superimposed on the optical mapping data depict wave propagation. The radially moving waves in A1 occur upon the onset of illumination. B, Opening of the optogenetically isolated circuit of conduction with non-illuminated areas (isthmi) of increasing width, such that escape of the trapped wave can occur. C, Voltage traces of three selected representative points showing trapped reentry with SR in the surrounding bulk tissue in A4 and escape of the reentrant wave through an isthmus in B8. D, Frequencies of all trapped excitation waves. E, Comparison between conduction velocities in different regions of the trapped reentry circuit (groups not significantly different from each other α=0.05 paired Wilcoxon signed rank test). F, Visualisation of a representative activation map that gave the data for E. G, Schematic representation showing how bridge-like funnel conduction velocities were measured (repeated for n=5 biological/technical replicates). H, Activation maps of non-illuminated and illuminated tissue in the set-up of G. I, Conduction velocities in function of width for bothe experimental set-ups: F in red, green, H in blue, orange (average ± standard deviation).

To show that the experimental trapped reentry circuits have source-sink mismatch at the funnel, 5 monolayers were illuminated with a rectangular strip having varying funnel widths (Figure 2G, Video V4). Activation maps were measured at 1Hz pacing for non-illuminated tissue and all funnel widths (Figure 2H) and the associated conduction velocities are plotted against funnel width (Figure 2I, blue and orange dots). The two different trapped reentry regimes (entrapment and escape from Figure 2F-8) are simultaneously visualized in the same plot (Figure 2I, green and red dots). Entrapment can be seen to start occurring for funnels with a width smaller than 0.13 cm (Figure 2I, projec-

tion down) and a curved excitation block border (more sink), while excitation waves still pass through funnel widths all the way down to 0.04 cm (Figure 2I, orange dots) when they have a less curved excitation block border (less sink).

3.3 Optogenetic vs fibrotic realization of trapped reentry

In real-life situations, conduction block can be a result of dense fibrotic regions. To show that there is a similarity in behavior between optogenetically created trapped reentry circuits and fibrotically created trapped reentry circuits, 2D simulations were performed (Figure 3). For a collection of isthmus openings, covering a variety of d_2/d_1 (isthmus outer opening length/isthmus inner opening length) ratio's (Figure 3A), both optogenetic conduction block (Figure 3B) and fibrotic conduction block (Figure 3C) were simulated. Either light was shone in the shape of the pattern onto optogenetically modified cells, or fibrotic cells were put in the shape of the pattern. The shapes were named d1-d10 for variations mainly in the average isthmus opening length, and a1-a5 for variations mainly in the angle of the isthmus. To show that the formation (only possible in the non-red-shaded areas), perpetuation and release of trapped reentry under sinus rhythm can be observed in both cases, the global sodium conductance was varied. To initiate such reentry, a dependence on frequency was observed for excitation waves to enter the circuit through the funnel (Figure S3), where higher frequencies sometimes skipped the circuit altogether (Video V5). However, once reentry is initiated, sub-panels B and C show a transition from 0% release towards 100% release. This transition happens when the d_2/d_1 ratio is decreased, but also when the sodium conductance is increased. While these transitions occur in both conduction block methods, they appear at different locations, indicating that the phenomenon of trapped reentry can be investigated in both configurations, but that the specifications are different. Both configurations also came with an excitable gap inside the circuit, but no resetting or entrainment was observed under external sinus rhythm pacing at different frequencies when reentry was ongoing (Video V6). These external excitation waves could only reach partially into the funnel (Figure 3D-E). To establish trapped reentry, the coupling effect between illuminated and non-illuminated cells (Figure 3D) caused funnel widths to be larger for the optogenetic case compared to the fibrotic one. However, the results suggest that optogenetic modelling of trapped reentry is valuable and that our experimental set-up is sufficient to capture the essence of the trapped reentry phenomenon. It also suggests that this phenomenon of trapped reentry could be found in real life under dense fibrotic circumstances.

3.4 Trapped Reentry in a 3D In Silico Model of Human Atria

To show how dense fibrotic tissue can be combined with realistic atrial geometries of the human heart, 3D simulations were performed in which the geo-

metric properties for trapped reentry from Figure 1 were created by transmural non-conducting fibrotic regions. A funnel-shaped isthmus was constructed (Figure 4A, Video V7) to connect the bulk of the tissue to the inner trapped reentry circuit in the right atrial wall of a realistic digital twin of the human atria (Figure 4B1-B2 and section 3.3 in the Supplemental Material). We used three

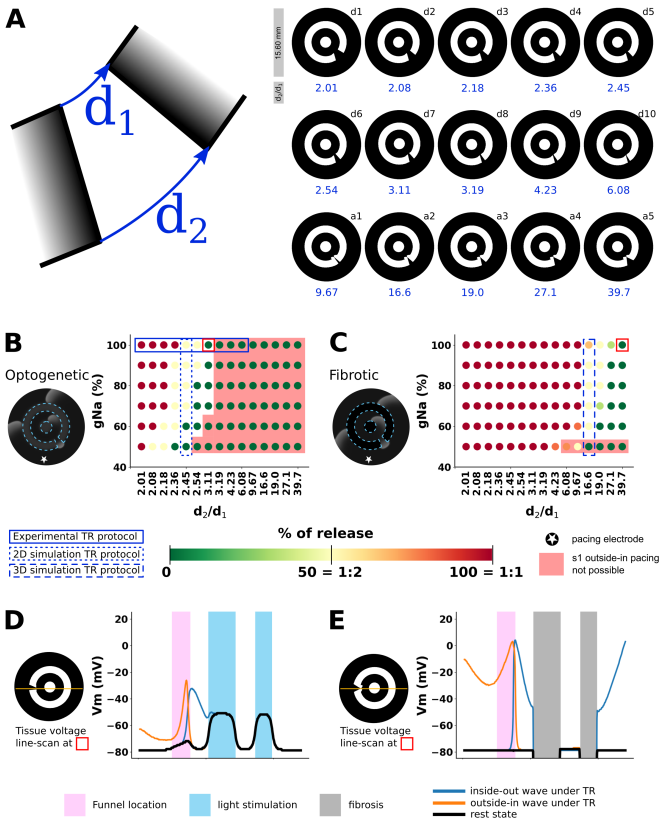

Figure 3 – **Optogenetic vs. fibrotic realization of trapped reentry.** A, The isthmus of a trapped reentry circuit can be characterized by the ratio of two distances (left). 15 geometries that were used with variable d_2/d_1 ratio are shown (right). B, Release percentage of a reentrant wave as a function of circuit geometry and sodium conductance when the geometry is realized through optogenetic conduction block. C, Release percentage of a reentrant wave as a function of circuit geometry and sodium conductance when the geometry is realized through fibrotic non-conducting regions. D-E, Tissue voltage line-scan through the isthmus under optogenetic and fibrotic conditions of trapped reentry.

models for human atrial cells, representing different stages of atrial remodeling: (1) the Courtemanche model[25] for healthy atrial tissue, (2) the AF Courtemanche model[26] representing paroxysmal AF, and (3) the Loewe model[27] for chronic AF. For each of these models, we found values of G_{Na} and G_{gap} causing

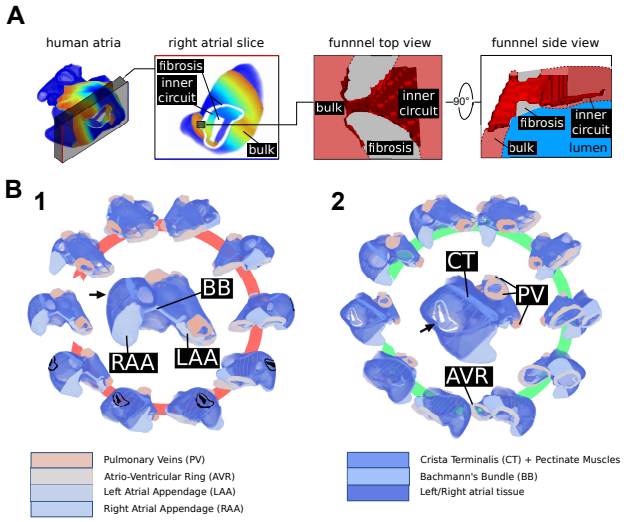

Figure 4 – **Design of the 3D funnel-shaped isthmus and the trapped reentry circuit in human atria.** A, 3D funnel-shaped isthmus between the circuit of trapped reentry and the bulk tissue. The funnel is gradually widening towards the inner circuit and has a sharp transition into the bulk of the atria. B, Rotating view of human atria with a circuit of trapped reentry. The central pictures are enlarged versions of the left most pictures in both panels. Atrial structures are indicated by different colors and labels. Non-conducting tissue is made transparent for better visualization. 1, Middle: anterosuperior view of the atria. For clarity, the circuit of trapped reentry is indicated in black. When not visible, circuit location is indicated with an arrow. 2, Middle: slightly tilted view relative to A that better visualizes the circuit of trapped reentry.

excitation waves to enter the isolated conduction circuit, to be trapped inside this circuit or to be released from the circuit (Figure 5A), i.e. conditions that imposed unidirectional block (for entry and trapping) and bidirectional propagation (for escape) at the isthmus.

Figure 5B summarizes the results obtained with different values of global GNa at 100% Ggap for each of the three atrial models (for details, see Table S1). In particular, global $G_{Na} > 31.4\%$ allowed propagation waves to enter the circuit from the outside for the Courtemanche model of healthy human atrial tissue (green bar). Waves rotating inside the circuit could not exit at global $G_{Na} < 41.3\%$ and only kept propagating for global $G_{Na} > 30.6\%$ (red bar). In the intersecting region, excitation waves could enter the circuit but could not escape from it (light green shading). Release of the reentrant waves could be accomplished by globally lowering Ggap but was only possible for points inside the green region surrounded by the dashed line. Similar results were obtained for the other two models (Figure 5B). The parameter range allowing release of trapped waves appeared to be largely independent of the length of the inner circuit although the escape frequency was higher for the longer reentrant circuits (Figure S4). Moreover, simulations at a higher spatial resolution (i.e.

100 μm) revealed larger parameter regions supporting trapped reentry (Figure S5).

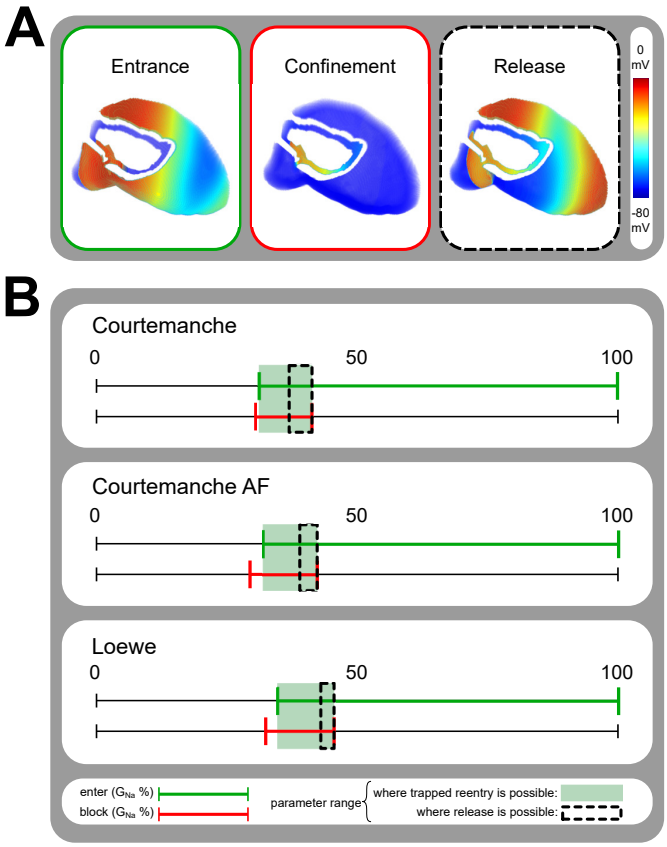

Figure 5 – **The conditions for trapped reentry differ between 3D models of healthy and diseased atria.** A, Overview of the three key aspects of trapped entry: entrance of an excitation wave into an electrically isolated circuit (left), confinement of the trapped wave inside the circuit (middle) and release of the excitation wave from the circuit (right). B, Conditions allowing entrapment and release of a reentrant wave from an isolated circuit. The upper lines in each panel indicate the range (in green color) of G_{Na} in which the wave can enter the circuit during SR. The lower lines indicate the range (in red color) of G_{Na} in which the wave can be trapped inside the circuit. The overlaps of both lines (light green boxes) mark the regions in which trapped reentry is possible. To release the reentrant waves, the gap junctional coupling efficiency is diminished. The regions in which release is possible are indicated by the dashed lines.

3.5 Clinical Translation

In a clinical setting, it is currently not feasible to record wave excitation patterns at the same spatial resolution as in simulations or in cardiac monolayer

cultures. Therefore, in realistic full atrial simulations (Loewe model) we calculated unipolar epicardial electrograms (Figure 6 and S6, Video V8 and V9) to derive clinically relevant data. In Figures 6 and S6, simulations of trapped reentry were run in a digital twin of human atria with a locally isolated conduction circuit located in the right atrium (as in Figure 4). These simulations spanned 12 seconds in real-time, which were divided in 4 sections of 3 seconds (Figure 6A and S6A, rows 1 through 4) with 3 images per second. SR was applied from the sinoatrial node at a frequency of 1 Hz for the duration of the simulation. Local reentry was initiated by timing an extrasystole (S2 pulse; horizontal red bars in Figure 6A and S6A, vertical red lines in Figure 6C-D and S6C-D) inside the electrically isolated region after a sinus pulse had entered. However, other initiation mechanisms might exist (Figure S7B).

To obtain trapped reentry, the active (G_{Na}) and passive (G_{gap}) properties of the tissue were changed based on our previous parameter analysis. The timing of these changes slightly differed between Figure 6 and Figure S6 to illustrate that trapped reentry can be induced directly (Figure 6) as well as after modification of the tissue properties (Figure S6). In Figure 6, sodium conductance was reduced after 3 seconds, i.e. before the S2 stimulus that trapped a wave. Subsequent reduction of the gap junctional coupling (after 9 seconds) led to escape of the reentrant wave from the isolated circuit (horizontal green bar in Figure 6A, green arrow in Figure 6B). In Figure S6, the sodium conductance was reduced after 5 seconds, which is after the S2 stimulus. As a result, the global reentrant driver that was established in the isolated circuit, became locally trapped after G_{Na} reduction. Escape of the reentrant wave from the isolated circuit again depended on a decrease (in this case after 10 seconds) of the gap junctional coupling. When the reduction in sodium conductance preceded the S2 pulse that initiated trapped reentry as in Figure 6, no irregular activity was observed through the unipolar electrodes in the bulk of the atria until the gap junctional coupling decreased. Contrarily, when trapped reentry was accomplished by applying an S2 pulse before decreasing the sodium conductance (Figure S6), two episodes of high-frequency pacing were observed. The first one occurred between the S2 pulse and the reduction in sodium conductance, while the second one emerged after the decrease of gap junctional coupling. For both simulations, epicardial unipolar electrograms were taken at 85 different locations in the atria (Figure 7, which is based on the simulations in Figure 6). Fundamental differences can be seen between electrograms recorded close to and far away from the circuit of trapped reentry. Far away from the dense fibrotic region, no influence of the trapped wave was seen (1 Hz signal) until the sudden onset of a fast pacing rhythm of 3.3 Hz after the reduction of gap junctional coupling. However, in a small region around the circuit of trapped reentry, fractionated atrial electrograms were observed as soon as trapped reentry was initiated.

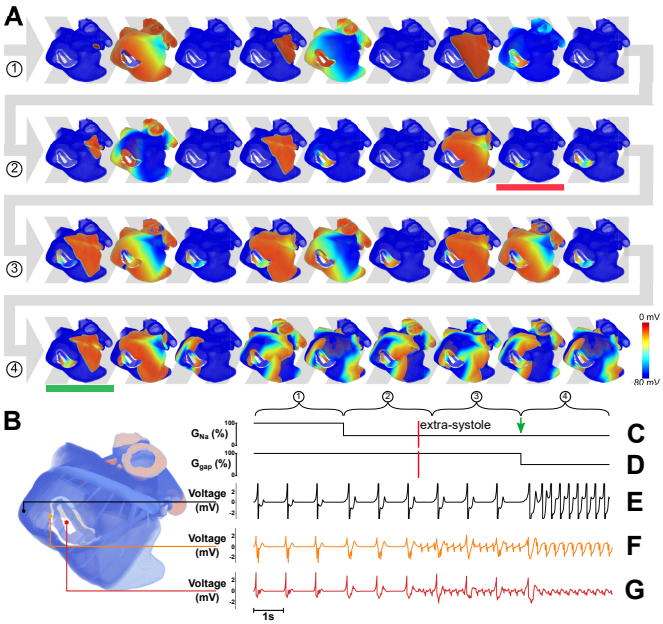

Figure 6 – **3D realization of trapped reentry linked to unipolar electrograms.** A, Visualization of the steps involved in trapped reentry through representative voltage maps (3 pictures/second, 12 seconds in total). The horizontal red bar denotes the moment an extrasystole and subsequent trapping occurs, while the horizontal green bar marks the escape of the trapped excitation wave. B, Enlargement of the human atria with anatomical regions indicated by different colors. C, Relative sodium conductance. D, Relative gap junctional coupling efficiency. E, Unipolar electrogram showing SR and tachyarrhythmia in the bulk atrial tissue. F-G, Unipolar electrograms next to the circuit of trapped reentry showing fractionation during SR.

4 DISCUSSION

The concept of trapped reentry relies on the temporal electrical isolation of a small region of excitable tissue wherein reentry can be established. Highly fibrotic regions are favorable for the establishment of such arrhythmias due to their many narrow conduction pathways. Trapped reentry can be explained by combining the theories behind impulse propagation block due to abrupt tissue expansion[30], and impulse transmission at narrow conduction pathways due to partial cellular uncoupling[20]. A circuit of trapped reentry thus typically consists of an electrically isolated region of excitable tissue connected to the bulk tissue through a narrow opening. This isthmus allows control over the excitation waves entering or leaving the reentry circuit through dynamic changes in electrophysiological tissue properties. Different realizations of such a circuit were demonstrated in both *in silico* and in vitro models. These models all contained two distinct regions of conduction block, the first one being the core of

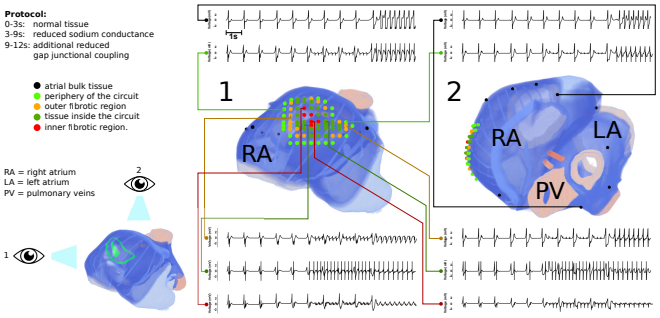

Figure 7 – **Unipolar electrograms recorded around the circuit of trapped reentry.** A total of 85 epicardial unipolar electrograms were taken, 10 of which are visualized for the process shown in Figure 6 with their location indicated on two different views of the atria (1, right lateral view; 2, superior view). Black: atrial bulk tissue, light green: periphery of the circuit, orange: outer fibrotic region, dark green: tissue inside the circuit, and red: inner fibrotic region.

the circuit, and the second one being a ring around the excitable tissue in the circuit, with an opening (the isthmus) allowing entrance and escape of excitation waves. The isthmus that connects the isolated region to the bulk of the tissue can be manipulated to influence source-sink relationships. This can be achieved by changing the active and passive electrical properties of the tissue[31] or by altering the geometrical properties of the isthmus through modifications of the inexcitable region that borders the circuit[32] (Figure 3). In our two 2D-models of trapped reentry, fibrosis was mimicked by means of optogenetically induced conduction block. Especially for establishing trapped reentry in vitro, the optogenetic approach was chosen since this technique allows full control over the parameters that influence source-sink mismatch. Another approach might be to use palmitoleic acid or other uncouplers to reduce gap junctional coupling[20]. This technique would be closer to the 3D realization of the studied phenomenon and better mimic what might be happening in ageing human hearts. This would require that the cells are seeded in specific patterns to create funnels of the desired shape, which is technically challenging. The optogenetic approach circumvents this problem. It should be noted, however, that the boundary of an optogenetically generated region of conduction block behaves differently from the boundary of a conduction-blocking fibrotic region. Due to its influence on neighboring cells, optogenetic depolarization resembles features of myofibrotic behavior, which can even be a source of ectopic foci[33,34]. Nevertheless, the similarity in behavior between optogenetically created circuits of trapped reentry in virtual and actual NRAM monolayers and circuits of trapped reentry delimited by fibrotic areas in virtual NRAM monolayers validates the modelling of trapped reentry using optogenetics (Figure 3). The monolayer studies further demonstrated that a tachyarrhythmia can exist locally with SR prevailing in the bulk of the monolayer and that this latent

arrhythmic source can be converted into an active driver with global impact. We have shown that this latent arrhythmic source is a phenomenon that can occur in atria containing cardiomyocytes with differently shaped action potentials representing healthy or electrically remodeled cells (Figure S4). When combining the results obtained with different circuits of trapped reentry and different computational cell models, several conclusions can be drawn.

1. For each mathematical/computational model, the $G_{Na} - G_{gap}$ parameter range allowing escape of trapped waves is similar for different-sized circuits (Figure S4). However, despite circuit length independence, it does depend on the geometry of the funnel that connects the circuit to the bulk of the atria (Figure 3).

2. The highest value of GNa at which escape of trapped waves can occur in our 3D models increases with the degree of tissue remodeling (Figure 5).

3. Funnels with higher ratios of funnel base cross-sectional area to funnel opening cross-sectional area allow escape of trapped waves at higher values of G_{Na} (Figure 3).

4. The 3D computational model of healthy atrial tissue did not allow the establishment of small circuits of trapped reentry in contrast to the 3D models of diseased atrial tissue with a shortened action potential duration.

5. When the wavelength of the trapped wave is close to the boundary length of the inner obstacle, the reentrant wave will either not escape or escape intermittently, e.g. during every second or third rotation (Figure S4).

6. At least two different ways exist to arrive in the trapped reentry regime. 1) A drop in sodium conductance to a fixed value (e.g. 45%), followed by atrial remodeling. 2) A gradual decrease of sodium conductance without a change (within a particular model) of the atrial cell properties. A combination of both these scenarios might also occur.

7. For the simulations in human atria, the changes in sodium and gap junctional conductance are in the range of those observed experimentally and computationally, in association with acute myocardial infarction, ischemia, commotio cordis, loss-of-function mutations and aging[35], i.e. an up to 97% reduction of G_{Na} [36–38] and an up to 55% decrease of G_{gap} [37,39].

In our simulation studies, we looked exclusively at changes in two specific global tissue properties (sodium conductance and gap junctional coupling) to pinpoint trapped reentry to a specific cause. We also purposefully chose a larger cross-sectional area and spatial resolution in our 3D model to exclude

any discretization effects, enabling us to ascribe the observed trapping and escape effects solely to these two global parameters. However, besides a reduction in sodium conductance and gap junctional coupling, there exist other source-sink modulators like changes in extracellular sodium concentration, a change in membrane resistance, a varying threshold potential due to a change in IK1 conductance, fibrosis and tissue geometry. Additionally, these changes don't have to be global, but can be local. The larger cross-sectional area (and associated larger circuit) that was used stands in contrast with previous *in silico* studies showing that lone sources of reentry might exist in dense fibrotic regions close to the percolation threshold. These studies[40,41] showed ectopic activity with small minimal cross-sectional areas (1 pixel) of the funnel opening to create unidirectional conduction block. As a consequence of our larger circuit, our electrograms only show continuous and monomorphic activity, while the random nature of the fibrotic tissue in the studies mentioned above[40,41] results in more fractionated electrograms, hinting at the possible existence of more severe cases than the focal arrhythmias we show (e.g. instant AF). Trapped reentry also represents just one example of a latent arrhythmia as one may assume that trapped ectopic foci can exist, in which a central ectopic source is surrounded by an outer fibrotic ring with an isthmus. The trapped reentry phenomenon might also have a link with sudden cardiac death due to ventricular tachyarrhythmias caused by the escape of trapped excitation waves. Altogether the probability of observing the phenomenon of trapped reentry in real life is probably larger than the current results suggest by implementing only global changes and remains subject for future investigation. Resembling certain features of our "trapped reentry" concept in vivo, it was shown both in dogs[42] and in humans[43] that adenosine and tetrodotoxin treatment caused so-called "exit block" of micro-reentries formed within the sinoatrial node. Micro-reentry has been shown to exist in the atrial wall as well[9], showing the potential for translational exploration. In favor of such translational exploration there exists additional clinical evidence of continuous abnormal behavior under SR[44]. So-called AF nests[12],[45] show regions with high-frequency electrical activity under SR. These highly resonant, localized atrial sites may harbor CFAEs during AF[12]. While AF nests and CFAE regions not always overlap[46], characteristics of both are present in trapped reentry circuits. It was also shown that in a healthy patient from the control group AF nests were found. AF induction was possible only in this patient despite having no history of spontaneous AF[12]. By targeting these AF nests as an extra measure, a lower AF-recurrence rate was observed in comparison with standard pulmonary vein isolation[45]. Another sign of trapped reentry after escape might be scar-related small reentries (SRSR) which can be detected by focusing on low-voltage fragmented electrograms[47]. One study found 7 of such SRSRs showing focal arrhythmia and was able to terminate these through focal ablation. We feel that more prospective (and retrospective, including AF nests and SRSRs) in vivo exploration should be part of dedicated subsequent studies that address efficient characterization, prognos-

tic features and clinical relevance. We foresee three relevant patient groups: 1) Patients with recurrent extra-PV triggers. After standard ablation in patients in sinus rhythm, trapped reentry may hide itself and only release waves in the form of extra PV-triggers. These trapped reentry circuits could get unmasked by drugs such as isoprenaline or adenosine. 2) Patients with recurrent AF that does not develop until years after ablation. During re-ablation, these patients are often found to display reconnection of pulmonary veins. Instead of these veins having been non-arrhythmogenic for all those years, it is also conceivable that a drop in gap-junctional coupling with age has caused the isthmuses between the veins and the atria to become conductive, causing the late development of atrial fibrillation. 3) Patients with an ablated atrial region that has a small surviving area within, with an isthmus connected to the surrounding tissue[48]. To detect trapped reentry in this group, first of all sinus rhythm during the procedure should not be caused by cardioversion, as this would also terminate trapped reentry. This might explain why AF termination during ablation has a better prognosis than cardioversion. To subsequently find these circuits, we would rely on high density grid catheters, which should be capable of capturing a trapped reentry circuit on a single catheter position when it is kept still for several sinus beats. However, it is not common to capture such a recording. Trapped reentry circuits might also get detected before onset of reentry by looking for small deflections in electrograms during sinus rhythm (Figure 6 and 6S). When doing so, clinicians should be extra careful to check whether there is pacing capture before labeling an area as scar tissue. After all, a trapped reentry circuit might get skipped (Figure S3) when operators perform atrial or coronary sinus pacing above sinus rhythm. AF-nests, SRSRs and fractionation during sinus rhythm combined suggest that latent arrhythmias could exist during SR and strengthens our idea that AF (recurrence) could be prevented through early recognition and treatment of trapped reentry circuits by combining HD-mapping techniques, better imaging, and correct patient selection. The recognition of trapped reentry as a possible source of arrhythmogenesis may therefore impinge on clinical practice. There have been studies in AF patients disproving the additional benefit of CFAE targeting over traditional methods[10]. In otherwise healthy patients, trapped reentry, which shows itself through CFAEs or regions of high-frequency electrical activity under SR (like AF nests), might be a predictor of future AF. Although detection of such CFAEs under SR is relatively infrequent[16], they are associated with potential lethal consequences, especially when escape of the reentrant waves causes them to affect the entire atria spreading over into the ventricles through extrasystoles. Hence, early targeting of these sources of abnormal conduction might prove valuable. The insight gathered in this study can aid the development of new ablation strategies that complement the current guidelines.

FUNDING This study was supported by The European Research Council (ERC Starting grant 716509) and the Netherlands Organization for Scientific Research (NWO Vidi grant 91714336), both to DAP. Additional support was

provided by Ammodo (to DAP and AAFdV).

DISCLOSURES None.

5 Supplementary Material

5.1 Experimental methods

1.1) Preparation of CatCH-expressing monolayers: Monolayers of neonatal rat atrial cardiomyocytes expressing Ca_{2+}-translocating channelrhodopsin (CatCh) were created. The hearts were excised from anaesthetized 2-day-old Wistar rats (RRID:RGD_737929). The atria were cut into small pieces and dissociated in a solution containing 450 U/ml collagenase type I (Worthington, Lakewood, NJ) and 18.75 Kunitz/ml DNase I (Sigma-Aldrich, St.Louis, MO). The resulting cell suspension was enriched for cardiomyocytes by preplating for 120 minutes in a humidified incubator at 37°C and 5% CO2 using Primaria culture dishes (BectonDickinson, Breda, the Netherlands). These cells were seeded on round glass coverslips (d = 15 mm; GerhardMenzel, Braunschweig, Germany) coated with fibronectin (100 μg/ml; Sigma-Aldrich) to establish monolayers. After incubation overnight in an atmosphere of humidified 95% air - 5% CO2 at 37°C, these monolayers were treated with Mitomycin-C (10 μg/ml; Sigma-Aldrich) for 2 hours to minimize proliferation of the non-cardiomyocytes. At day 4 of culture, the neonatal rat atrial cardiomyocyte monolayers were incubated for 20-24 hours with CatCh-encoding lentiviral particles at a dose resulting in homogeneous transduction of nearly 100% of the cells. Finally, the cultures were washed once with phosphate-buffer saline, given fresh culture medium and kept under culture conditions for 3-4 additional days. 1.2) Optical mapping and optogenetic manipulation: Optical voltage mapping was used to investigate trapping and releasing of excitation waves in the CatCh-expressing monolayers on day 7 of culture by using the voltage-sensitive dye di-4-ANBDQBS (52.5 μM final concentration; ITK diagnostics, Uithoorn, the Netherlands). Optical data were acquired using a MiCAM ULTIMA-L imaging system (SciMedia, CostaMesa, CA) and analyzed with BrainVision Analyzer 1101 software (Brainvision, Tokyo, Japan). Only monolayers characterized by uniform AP propagation at 1-Hz pacing and homogeneous transgene expression were included for the optogenetic investigation (n=8). CatCh was locally activated by using a patterned illumination device (Polygon400; Mightex Systems, Toronto, ON) connected to a 470 nm, high-power collimator light-emitting diode (LED) source (50 W, type-H, also from Mightex Systems). PolyLite software (Mightex Systems) was used to control the location of the areas of illumination. 1.3) Trapped reentry initiation: The set-up for the experimental initiation process of trapped reentry is shown in Figure S1. The movie frames depicted at the bottom denote the patterns that were uploaded into the patterned illuminator that resulted in the representative optical mapping samples of Figure 2 which show the effect of the change

in pattern. Underneath we present all the different patterns in the initiation process of trapping and releasing a reentrant wave one by one:

1. Pattern 1 shows the closed reentry circuit, which upon realization through patterned illumination, initially creates outward waves that move away from the illuminated area. Once these waves have passed, an effective non-conducting area has been established where the light shines.
2. Pattern 2 shows the S1 pulse; the bridge between the outer illuminated ring and the inner illuminated core, which initializes waves in both directions of the circuit, which will bump into each other and annihilate each other at the opposite side in the circuit. At the place of illumination, a small region of depolarized cells will make another small non-conducting area.
3. Pattern 3 shows the same pattern as pattern 2, but slightly wider on the left side. This pattern will be changed to when the tissue on the left of the S1 pulse is able to excite again. As a result, a single wave will be initialized that runs counterclockwise, but gets blocked in the clockwise direction due to the illuminated depolarized area causing conduction block.
4. Pattern 4 shows the removal of the small inner circuit light block. This allows the wave that was created with pattern 3 to freely go around the middle obstacle and create a reentry. Sinus rhythm is generated in the outer area around the blue non-conducting ring.
5. Pattern 5 is a copy from pattern 4, where there is a reentry present in the inner circuit.
6. Pattern 6 shows a tiny space that was left in the outer light boundary. This gives a little area where conduction is possible again. However, this region is too narrow and the reentrant wave cannot escape.
7. Pattern 7 has the space from pattern 6 increased and the conduction area is just wide enough such that the source-sink mismatch can be overcome and the reentrant wave can escape.
8. Pattern 8 shows an even wider gap in the outer light band, where there is clear release of the reentrant wave on every rotation around the middle light obstacle.

5.2 Computational methods

Simulation set-up:

The numerical solver was implemented with the C and C++ programming languages, using the CUDA toolkit for performing the majority of computations

on graphical processing units. Visualization of results was done with the help of the Python programming language and ParaView (Kitware). Computations were performed with single precision and run on an AMD Ryzen Threadripper 2950X 16-Core machine with two GeForce RTX 2080 Ti graphics cards. For the simulations of the whole atria with a spatial resolution of 150 *mu*m and 100 *mu*m, one graphical processing unit did not suffice to store all the variables needed in the computation. By making use of unified memory, available on the newest NVIDIA architectures, it was possible to run simulations on two GPU units that are coupled.

Cell models:

Different cell models were used for 2D and 3D simulations of the trapped reentry phenomenon. These models can be found underneath: *Majumder et al.*: The 10 major ionic currents that make up I_{ion} in (Eq. 1 of the main manuscript) are:

$$I_{ion} = I_{Na} + I_{CaL} + I_{K1} + I_{to} + I_{Ksus} + I_{Kb} + I_{Nab} + I_{Cab} + I_f + I_{KAch} \quad \text{(S1)}$$

Here, the different cardiac currents are represented as follows: the fast Na^+ current (I_{Na}), the L-type Ca^{2+} current (I_{CaL}), the inward rectifier K^+ current (I_{K1}), the transient outward K^+ current (I_{to}), the sustained outward K^+ current (I_{Ksus}), the background K^+ (I_{Kb}), the background Na^+ (I_{Nab}) and the background Ca^{2+} (I_{Cab}) currents, the hyperpolarization-activated funny current (I_f), and the acetylcholine-mediated K^+ current (I_{KAch}). Units for conductance measurements (G_X) and measurements of intracellular and extracellular ionic concentrations ($[X]_i$ and $[X]_o$), are in nanosiemens per picofarad (nS/pF) and millimole per liter (mM), respectively. *Courtemanche et al., Loewe et al.*: In all three cases of the human atrial model, the total ionic current is given by:

$$I_{ion} = I_{Na} + I_{CaL} + I_{K1} + I_{to} + I_{NaCa} + I_{NaK} + I_{Kr} + I_{Ks} + \\ + I_{bNa} + I_{bCa} + I_{pCa} + I_{Kur}$$

Here, the different cardiac currents are represented as follows: the fast Na^+ current (I_{Na}), the L-type Ca^{2+} current (I_{CaL}), the inward-rectifier K^+ current (I_{K1}), the transient outward K^+ current (Ito), the Na^+/Ca^{2+} exchanger current (I_{NaCa}), the Na^+/K^+ pump current (I_{NaK}), the rapid-delayed rectifier K+ current (I_{Kr}), the slow-delayed rectifier K^+ current (I_{Ks}), the background Na+ current (I_{bNa}), the background Ca^{2+} current (I_{bCa}), the plateau Ca^{2+} current (IpCa), and the ultra-rapid-delayed rectifier K^+ current (I_{Kur}). Units for conductance measurements (G_X) and measurements of intracellular and extracellular ionic concentrations ($[X]_i$ and $[X]_o$), are in nanosiemens per picofarad (nS/pF) and millimole per litre (mM), respectively.

Simulation technical details:

Simulations were performed both in 2D and 3D, each of which had different technical specifications as they were performed with different cell models.

Monolayer: In the two-dimensional monolayer system, isotropy was assumed, and thus the conduction tensor takes on a diagonal form with identical elements. Therefore **D** reduced to a scalar in our calculations, with a value of 0.00012 cm^2/ms. This resulted in a signal conduction velocity of 19 cm/s. It has been shown before that anisotropy in monolayers amounts to a rescalint of the resulst in a homogeneous monolayer[49], which is why simulations were performed in homogeneous tissue.

Eq.1 was integrated in time using the forward Euler method with time step $\Delta t = 0.005$ ms, and in space, using the centered finite-differencing scheme with space step $\Delta x = \Delta y = 0.003215$ cm, subject to "no flux" boundary conditions. The simulation domains contained 512 x 512 grid points, such that the physical size of the simulated tissue was 1.646×1.646 cm^2. The gating variables in the electrophysiological model for the neonatal rat cardiomyocyte were integrated using the Rush and Larsen scheme[50]. *Whole organ*: Owing to the natural anisotropy of realistic cardiac tissue, the elements were computed on the basis of a reconstructed fiber direction field. The transverse diffusion coefficient (Dt, for signal propagation across the fibers) was assumed to be 9 times less than the longitudinal diffusion coefficient (Dl, for signal propagation along the fibers). Elements of the diffusion tensor were computed as follows:

$$D_{ij} = (D_l - D_t)\alpha_i\alpha_j + D_t\delta_{ij} (Eq.S3)$$

where α_i are components of the unit vector that is oriented along the direction of a fiber. We used $D_l = 1.54$ cm^2/s. This resulted in a conduction velocity of 72 cm/s along the fiber direction. Eq.1 was integrated in time using the forward Euler method with time step $\Delta t = 0.01$ ms, and in space, using the centered finite-differencing scheme with space steps $\Delta x = \Delta y = 0.0300$ cm, 0.0150 cm and 0.0100 cm in whole atria, subject to "no flux" boundary conditions. The simulation domains for the whole atria contained 2.173.891, 17.391.128 and 58.695.057 grid points, respectively for a resolution of 300 *mu*m, 150 *mu*m and 100 *mu*m. The gating variables in the electrophysiological model for the human cardiomyocyte were integrated using the Rush and Larsen scheme[51].

APs of atrial cell models:

The simulations were carried out with three different models (Figure S2), each of them describing a different stage in atrial remodeling. When simulating with realistic cellular models, they have to be pre-paced such that they settle into an APD that doesn't change from beat to beat. This was done by delivering 50 pulses at a frequency of 1 Hz at the single-cell level, after which their parameters were used to initialize all cells in the 3-dimensional models. The APs of all

three models after 50 pulses at the single-cell level have been portrayed here. A healthy atrial cell has an action potential with a notch-dome look and is described by the Courtemanche model[25]. Under AF remodeling, modelled by the Courtemanche AF model[25], the APD shortens and the AP looks triangular, with slow repolarisation. Under chronic AF remodeling as described by Loewe[27], the AP stays initially at a higher potential, but has fast repolarization, making its APD_90 shorter than the AF remodeled AP. These differences in AP make for different dynamics in reentry circuits, most notably that atrial remodeling allows smaller reentry circuits to exist due to shorter APDs.

Electrogram computation:

Because of the monodomain formulation of the cell models, Im from Eq. 2 in the main manuscript is readily available and allows us to compute the extracellular potential ϕ_e. Since ϕ_e is linearly related to V_m, it is computed for practical reasons as a weighted sum of the membrane potential V_m using the discretized diffusion operator already defined to solve the propagation equation (Eq.1 in the main manuscript).

5.3 Electrically isolated circuit design methods:

2D Funnel Opening Design:

The funnel connecting the inner region of the trapped reentry circuit to the bulk tissue can be characterized by means of two lengths (Figure S3A). These are the arclengths of the funnel along the inner and the outer radius of the funnel, denoting the surfaces where the funnel touches the inner circuit and the bulk of the tissue respectively. The ratio between these two lengths gives a measure for the source-sink mismatch that is present in a particular funnel. The funnel that was used for the simulations in Figure 1 can be seen having a d_2/d_1 ratio of 2.38. By making d_2 larger than d_1, a somewhat triangular shape can be made where the base of the triangle is on the outside. When you go from outside the circuit to inside, you will encounter each time less and less cells, which ensures that there will always be enough source to feed the sink and hence wave propagation. When you go from inside to outside however, the cells constantly have to excite more cells than are currently excited. This makes that there is more sink than source in that situation, which might cause wave propagation block.

3D Funnel Opening Design:

The design of the three dimensional funnel that was used in all simulations has been visualized in Figure 3 and Supplementary Video V4. The leftmost panel shows an image of the whole human atria. When we zoom in on a specific part of the right atrium, we are able to clearly see one of the circuits that was used for

trapped reentry. On the left side of the circuit, the opening can be seen. This opening is of crucial importance to accomplish the effect of trapped reentry. The top view of the funnel can be seen in the third panel, upon zooming in on a specific region of the circuit. For visualization purposes, only a contour has been plotted. Therefore, to the left of the opening there is still the bulk of the atrium full of myocardial cells. On the right is the reentry circuit, also full of myocardial cells. Upon going from outside to inside the circuit, a slow increase in width of the funnel was designed which connects to the circuit. This allows for the cardiac excitation wave to enter since slow increases can be overcome when the sodium conductance level drops. When going from inside to outside on the other hand, at first there is a slow decrease in funnel width, which suddenly opens into a large area. Due to the source-sink mismatch, this sudden opening towards a bulk of cardiomyocytes will cause conduction block. To increase the amount of myocytes that become available for the excitation wave, the exit of the funnel has been designed to have a sharp angle with the funnel wall. Both taken together, this makes for unidirectional conduction block under the right circumstances. The side view of the funnel can be seen in the last and fourth panel. The top of that picture is at the epicardial side of the atria, while the bottom is at the endocardial side. This time when going from outside to inside, you can see a smaller increase in the funnel height than in the width due to the small wall thickness of the atria. When going from inside to outside the circuit on the other hand, there is first a slow decrease in the funnel height after which a sudden increase happens by means of a vertical cut-off, or a right angle of the exit wall with the funnel wall. To determine the radius that was needed for obtaining block in a two-dimensional and three-dimensional funnel, we based ourselves on Thomas et al.[51]. The smallest width of the funnel as it can be seen in the third panel is 7 voxels, which under the spatial resolution of 150 *mu*m comes down to 1.05 mm. The smallest height of the funnel on the other hand is 8 voxels, which amounts to 1.20 mm. The minimal cross sectional area of the funnel is therefore 1.26 mm^2. While this is rather large and *in vivo* scenarios will include smaller minimal cross-sectional areas, this larger area was chosen on purpose to exclude any possible discretization effects. Due to the larger opening we are now able to ascribe the observed effects solely to the reductions in sodium conductance and gap junctional coupling. The values that were used for the funnel opening are also dependent on the fiber orientation inside the atria. Therefore, depending on the orientation of the circuit in the atria, the funnel opening will need to be slightly modified. In this example the fibers are oriented from the upper left corner towards the lower right corner in the second and third panel of Figure 3.

Trapped reentry circuit in full human atria:

To get a better feel of the geometry of the whole human atrium, a rotational view was provided (Figure 4). The atria show all different anatomical regions

in a different color. Those familiar with the atrial anatomy will easily distinguish the crista terminalis, Bachmann's bundle, pulmonary veins, pectinate muscles, and the right and left atrial appendages. In both panels, a trapped reentry circuit was included in the right atrial wall. The non-conducting regions in these circuits are modelled by means of fibrotic tissue, which was made see-through for better visualization of the geometry. The human atria in the model have dimensions of 10.755 cm × 8.895 cm × 7.035 cm. The size of the circuit (inner obstacle plus conducting region) is 2.694 cm x 1.8375 cm × local wall thickness 4.95 cm^2 × local wall thickness, and of the inner obstacle is 1.410 cm × 0.468 cm × local wall thickness 0.66 cm^2 × local wall thickness. Figure 4A shows the atria in its conventional view. In the center of the circle, a frontal view of the atria can be seen, with clear right atrium (left side of the figure), left atrium (right side of the figure) and pulmonary veins (orange regions). Around it, a full rotation can be seen, where the back of the atria shows the coronary artery. Unfortunately, in this view the trapped reentry circuit that was introduced is barely visible.

Therefore, an additional view on the atria was provided in Figure 4B. Here, the atria have been turned in such a way that the circuit becomes best visible. This entails a more aerial view. Also here, the atria have been turned a full rotation, thereby also showing the valves when the view from underneath is seen.

5.4 Trapped Reentry parameters motivation and methods:

Enabling or disabling wave escape based on source-sink mismatch:

To motivate our choice for the design of the entrance to the trapped reentry circuit, as well as the changes in global parameters that were investigated in the manuscript, it is useful to take a look at the key concept of the source-sink relationship related to the propagating activation wavefront[52]. A wavefront can propagate as long as unexcited but excitable cells (the "sink") have their *sodium channels* activated by the diffusion current moving forward from depolarized cells at the leading edge of the front (the "source"). On the other hand, the *gap junctional coupling* (mediated through the diffusion current) acts as a drain on the source. If a relatively small source is attached to a larger sink, the loss of source current caused by the sink may reduce the current available for excitation to the point that propagation fails. This indicates a critical relationship between the source current for excitation and the mass of tissue being excited, which drains the source current electrotonically. This principle can be used to create an isthmus capable of unidirectional block under the right circumstances. This can be accomplished in two ways: 1) through ionic changes 2) through geometrical changes. We first take a closer look at the ionic changes that can create unidirectional block. If we reduce the sodium channel conductance ($G_{Na} \searrow$), the sink excitation gets reduced which results in blocking of the

wave at the opening. On the other hand, if we reduce the gap junctional coupling ($G_{gap} \searrow$), there is a longer exposure of the cells in front of the wavefront to the diffusion current such that the source doesn't get immediately drained, making propagation possible again. Another possibility lies in changing the geometry of the opening. If the d_2/d_1 ratio gets increased for the funnel (Figure 3), more sink is created than there is source for the outgoing wave. When this ratio becomes large enough, conduction block will happen. This process can be reversed by making the ratio smaller again.

The described processes give rise to realistic situations[37] that can create trapped reentry *in vivo*. The first one is a decrease in sodium conductance combined with an ectopic pulse to initiate trapped reentry[31,32,35,53,54], and a reduction in the gap junctional coupling to release[36,55] the trapped waves (Figure 1, 5, 6, S6). The second one would be one where the fibrotic pattern grows in such a way that it creates a funnel as an opening with unidirectional block. In combination with an ectopic pulse, this gives once again rise to trapped reentry. The fibrotic pattern can however grow in such a way that the opening of the funnel on the outside becomes smaller, opening the way for escape of the trapped waves (Figure 2). Combinations of these two proposed ways are possible as well.

2D Trapped reentry technique comparison:

It was mentioned that there is a similarity in behavior between optogenetically created trapped re-entry circuits, both *in silico* and *in vitro*, and fibrotically created trapped reentry circuits in realistic human atrial models. This has been shown in 2D simulations (Figure 3), and suggests that optogenetic modelling of trapped reentry is valuable.

With the use of subpanels B and C it is also possible to show the difference between the protocols that were used to induce trapped reentry in different settings. For the experimental trapped reentry protocol (dots circled with a solid blue line) we made use of the optogenetic approach. We kept the tissue at its normal conductance levels, but changed the isthmus width (and hence the d_2/d_1 ratio), where we effectively went from a high ratio to a low ratio, thereby releasing the wave. For the protocol that was used for the 2D simulations, we worked once again with optogenetics. The pattern that was used was geometry d6 with a d_2/d_1 ratio of 2.38. We varied sodium conductance, where trapping occurred when this parameter was lowered. For the 3D simulations, we used the fibrotic approach. Also here, trapping occurred when lowering the sodium conductance level.

2D Trapped reentry technique comparison:

It was mentioned that there is a similarity in behavior between optogenetically created trapped re-entry circuits, both in silico and in vitro, and fibrotically

created trapped reentry circuits in realistic human atrial models. This has been shown in 2D simulations (Figure 3), and suggests that optogenetic modelling of trapped reentry is valuable. With the use of subpanels B and C it is also possible to show the difference between the protocols that were used to induce trapped reentry in different settings. For the experimental trapped reentry protocol (dots circled with a solid blue line) we made use of the optogenetic approach. We kept the tissue at its normal conductance levels, but changed the isthmus width (and hence the d_2/d_1 ratio), where we effectively went from a high ratio to a low ratio, thereby releasing the wave. For the protocol that was used for the 2D simulations of Figure 1, we worked once again with optogenetics. The pattern that was used was geometry d6 with a d_2/d_1 ratio of 2.38. We varied sodium conductance, where trapping occurred when this parameter was lowered. For the 3D simulations, we used the fibrotic approach. Also here, trapping occurred when lowering the sodium conductance level.

2D Trapped reentry influence of sinus wave frequency:

Entering a trapped reentry circuit gives a small deflection in the electrogram signal when you measure right on top of it. To see whether a trapped reentry circuit could be detected early on through sinus pulses alone, we set out to pulse the neonatal rat atrial cardiomyocyte tissue under optogenetic and fibrotic excitation block conditions at different frequencies (Figure S3). We observed that under certain frequencies, the circuit got skipped altogether and is rendered "invisible". The location of sinus pacing in a well together with the two possible outcomes of entering or skipping the circuit, are shown in Figure S3A. A decreasing trend was observed in entering percentage when pacing at higher frequencies (Figure S3B), meaning that the circuit gets skipped at higher frequencies. A complete analysis of 4 selected frequencies (2, 5, 10 and 12.5 Hz) in all funnels under a variation in sodium conductance, is shown in Figure S3C. These results imply that trapped reentry circuits might get missed altogether when looking for them.

3D Trapped reentry parameter details:

Trapped reentry was realized in two different reentrant circuits in the human atria. The opening of these circuits remained the same (Figure 3), but the inner circuit was changed such that the travel time of the waves would be different for one revolution through the circuit. The circuits can be seen in Figure S4 on the left. The top circuit supports reentry at higher frequencies (4.7 Hz) than the lower one (2.9 Hz). For both circuits, all three human atrial models were tested. All three of them represent different stages in arrhythmia development: Courtemanche[25] for healthy atria, Courtemanche AF[26] for atrial fibrillation, and the Loewe[27] model for chronic atrial fibrillation which denotes a more severe stage. The images that are shown on the left are both visualizations of the

release phase under the Courtemanche AF model. These graphs give details about the underlying datapoints that were the foundation for Figure 5. On the x-axis, you are able to see the percentage of the gap junctional coupling. The y-axis shows the percentage of sodium conductance in comparison with the standard value. In each graph the top line of points shows the largest value of sodium conductance for which it was possible to trap the wave. Under 100% of the diffusion coefficient, it can be seen that the wave is indeed trapped since the point is colored green in each graph. Upon reducing the diffusion coefficient 50% is released, which turns into 100% release upon further increase and eventually results in conduction block upon even further decrease. Measurement points were taken for every 10% of diffusion, and every 1% of G_{Na}. The upper boundary of G_{Na} was also included, which was measured at a sensitivity of 0.1%. To construct Figure 5, we looked at the regions where both 50% and 100% escape were possible to deduce the range of diffusion coefficients for which release was possible. This because it was shown that upon enlarging the circuit, all 50% release points would become 100% release points. More details about the parameters for trapped reentry can be found in Table T1. It contains all the values that resulted from scanning for all stages of trapped reentry: entering the circuit, trapping the excitation wave, and releasing the excitation wave. The long circuit is the one that can be seen in the bottom row of Figure S4, while the short circuit is the one from the top row. In Table T1, G_{Na}-S2 is the sodium conductance level that was needed to allow a wave to be trapped inside the circuit after the S2 ectopic pulse that is needed to initiate reentry. Details for the last four rows in the table were provided in Figure S4.

3D Trapped reentry spatial resolution:

In Figure S4, no mention was made about the lower boundary of the parameter range. This is because the lower range is mainly determined by the spatial resolution at which simulations are carried out. To show this, parameter ranges were calculated for two different spatial resolutions: 150 mum, and 100 mum. This was done for the upper circuit that was shown in Figure S4 where the Courtemanche AF model was chosen to do all simulations. The results are visualized in Figure S5. The top row shows the trapped reentry circuit in a three-dimensional slice of the right atrium. The spatial resolutions are mentioned above each figure. The size of the geometry is related to how many points are inside the simulation domain. For a small space-step or high spatial resolution, more cells will be needed to simulate the full circuit. To carry out these large simulations, we resorted to computing on two GPUs simultaneously.

3D Unipolar electrograms overview:

Unipolar electrograms were not only taken at the three points depicted in Figure 6 and S6 in the main manuscript. In total 85 electrograms were taken at

the epicardial surface of the atria. They were placed in selected areas. For the stimulation protocol that was used for Figure 6 and S6, 10 representative electrograms have been shown in Figure 7. These selected electrograms come from 6 different areas which are color coded in the figure (red, dark green, orange, light green, black). Each color corresponds to a different structural part in the trapped reentry circuit. These different regions each have particular specific characteristics that can be seen in their electrograms:

1. red: This denotes the inner fibrotic region of the reentry circuit. Here, no direct propagation of an electrical signal is witnessed. However, the far field effects of the circuit as well as the sinus pulses are visible on the electrograms and display fractionated behavior.

2. dark green: Conducting tissue inside the reentry circuit. In these electrograms, it is possible to see the high frequency of wave propagation once trapped reentry has been initialized.

3. orange: The outer fibrotic region of the reentry circuit is indicated with this color. Just like in the case of the red colored electrograms, here the results are based on the far field effect. Fractionation due to trapped reentry can also once again be observed.

4. light green: This region is just outside the reentry circuit, but already inside the bulk tissue of the atria. Here it should be noted that although these points are extremely close to the reentry circuit, the resulting electrograms show barely any sign of trapped reentry occurring, but instead show predominantly atrial sinus rhythm. These electrograms make clear that the effect of trapped reentry can easily go unnoticed.

5. black: These points are far away from the reentry circuit (some even in the other atrium). Here, absolutely no sign is shown of the presence of the trapped reentry circuit. This showcases that a dormant arrhythmia might be present in the atria while the majority of electrogram signals display sinus rhythm.

It has to be noted that there is a drop in amplitude for the orange and red signals. This is a direct result of the electrode not connecting to conducting tissue and therefore only picking up far field effects. All other regions show high spikes whenever the propagation wave passes.

Alternative methods to create a trapped reentry circuit:

To explain the principle of trapped reentry, it was mentioned that one ectopic beat was needed to create a reentrant circuit to start trapped reentry. However, it has been shown that other mechanisms might be able to initiate this process as well, such as the occurrence of two ectopic foci within the circuit[56].

Other possibilities exist as well (Figure S7). It is possible to denote a circuit with the use of terminology from electrical circuits. As an equivalent symbol for the sino-atrial node (SAN) which periodically sends propagation waves into the bulk atria, a circle was taken with in it a simplified action potential. Funnels capable of unidirectional block can be compared to diodes (triangle with line). In an electrical circuit, a diode can be overcome by providing a large enough voltage to overcome the block, similar to how we are able to influence the source-sink mismatch.

With these pictorial representations, it is now easy to make schematic pictures of other possibilities to create trapped reentry. One of these possibilities is to have two regions of unidirectional block. One would be at the entrance of the circuit and another one would be within the circuit. In this way, it is possible for the reentry to establish from a wave originating from the SAN without needing an S2 interference. Another possibility would be where multiple entrances are present, although they must all have the property of unidirectional block. By means of the interplay of arrival times to the different entrances, this might also constitute an alternative way of initiating the trapped wave. More possibilities can be found, but these extra possibilities for the creation of a trapped reentry circuit indicate that the chances for observing this phenomenon are larger than what is shown here.

5.5 SUPPLEMENTARY FIGURES AND FIGURE LEGENDS

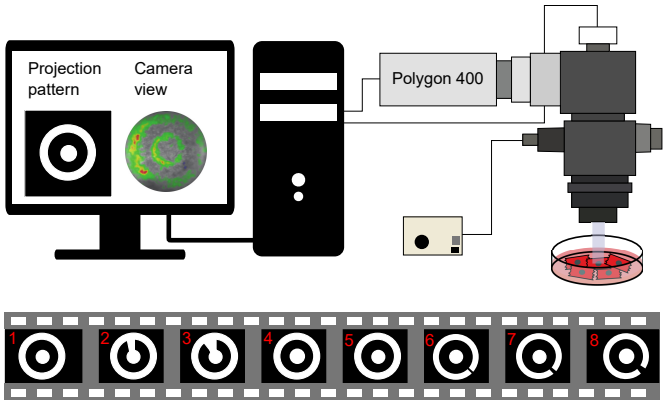

Figure S1 – **Experimental set-up.** Schematic view of the optical mapping set-up that was used to carry out the experiments. The patterned illuminator (Polygon 400) shines light according to the patterns depicted in the 8 movie frames to trap and release a reentrant wave.

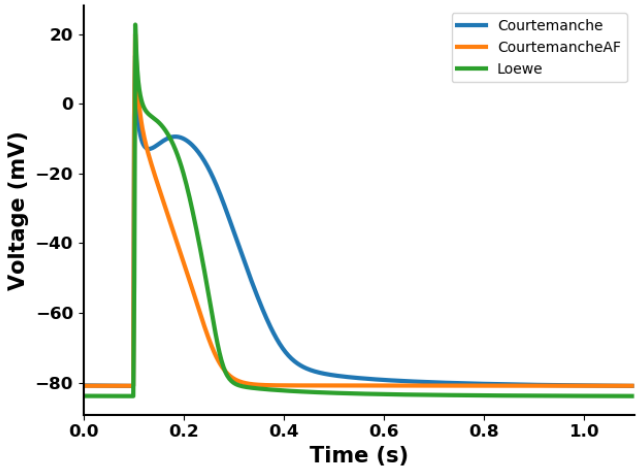

Figure S2 – **Atrial APs.** AP-shapes of the three different atrial models that were used after 50 initiation pulses at 1Hz. Each model represents a different stage of remodeling.

5.6 TABLES AND SUPPORTING INFORMATION

5.7 LEGENDS FOR VIDEO FILES

Video V1: 2D In Silico Trapping and Release: Two dimensional in silico optogenetic trapped reentry (circuit with $d_2/d_1 = 2.45$ from Figure 3) and excitation release can be seen for a cardiomyocyte culture model under different gap junctional couplings (Top row) and different sodium conductances (bottom row). Blocking (0% release), full release on every rotation (100% release) and intermediate regimes (e.g. 25% release) can be seen. (Figure 1).

Video V2: Experimental Trapping in a Cardiomyocyte Culture: Essential steps of the experimental realization of trapped reentry (Figure 2). Voltage signals are made visible by means of a fluorescent dye. Timer indicates real-time elapsed seconds. Patterns at the bottom that light up show the light pattern and conduction block present at that moment.

Video V3: Sinus Rhythm under Experimental Trapping in a Cardiomyocyte Culture: Long version of the experimental realization of trapped reentry. Voltage signals are made visible by means of a fluorescent dye. Sinus pulses are indicated by text. Timer indicates real-time elapsed seconds. Patterns at the bottom that light up show the light pattern and conduction block present at that moment.

Video V4: Sinus rhythm through a narrow funnel in a Cardiomyocyte Culture: Experimental realization of a wave going through a funnel (0.07 cm) with a straight border. Voltage signals are made visible by means of a fluores-

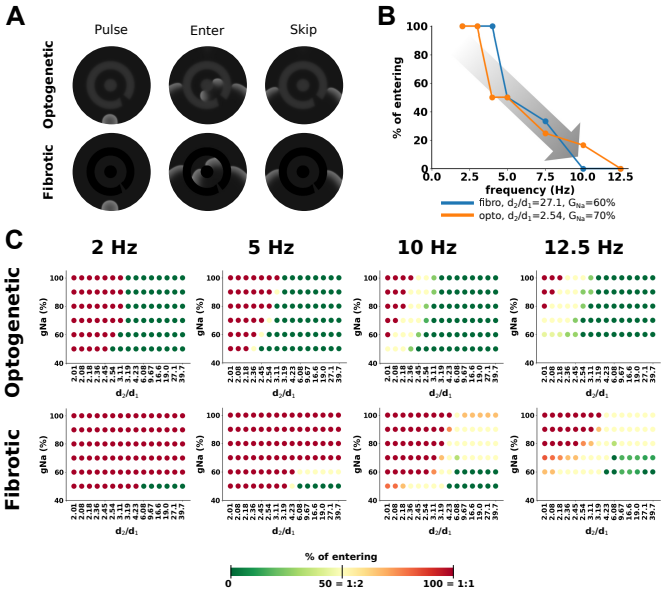

Figure S3 – **Sinus wave frequency effects.** Visualization of the sinus pulsing location together with its two possible outcomes: entry of the circuit and skipping of the circuit. B, Percentage of sinus waves that enter the circuit decreases with increasing pulsing frequency. C, Percentage of sinus waves that enter the circuit in function of the funnel opening (shown in Figure 3) and the sodium conductance.

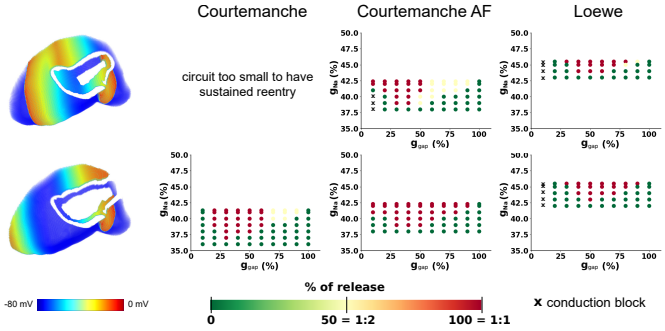

Figure S4 – **Detailed parameters for trapping and releasing of excitation waves.** Details of the regions of trapping and releasing for both circuits that were tested. For each circuit, results for all three tested human atrial models are shown (Left to right: Courtemanche, Courtemanche AF, Loewe).

cent dye. Sinus pulses are indicated by text. Timer indicates real-time elapsed seconds.

Video V5: 2D in silico circuit skipping under sinus rhythm in silico:

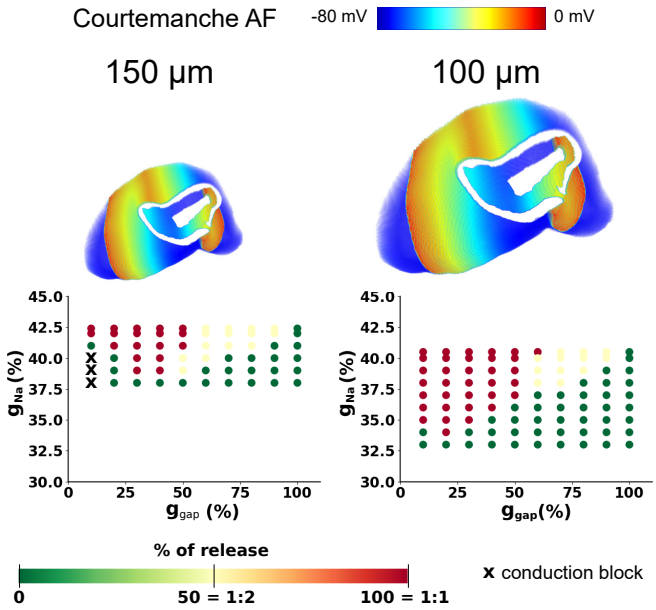

Figure S5 – **Different conditions for trapped reentry depending on the resolution with which simulations are run.** Details of the regions of trapping and releasing for both circuits that were tested. For one circuit, results for the two tested spatial resolutions are shown(left: 150 umm, right: 100 umm).

Sinus pacing for 2s where not a single wave enters the trapped reentry circuit (optogenetic circuit with d2/d1 = 3.11 from Figure 3, fibrotic circuit with d2/d1 = 39.7 from Figure 3). Timer indicates real-time elapsed seconds.

Video V6: 2D in silico sinus rhythm cannot enter a trapped-reentry circuit: Trapped reentry initialization with an S1-pulse outside the circuit for circuits realized with optogenetic and fibrotic conduction block (optogenetic circuit with d2/d1 = 3.11 from Figure 3, fibrotic circuit with d2/d1 = 39.7 from Figure 3). After letting the reentry settle (2s), sinus pulses were given at various frequencies for a duration of 5s. Timer indicates real-time elapsed seconds.

Video V7:3D Funnel Design: Three dimensional rotational view of the funnel that was used to connect the circuit to the bulk of the atria in realistic whole atria simulations (Figure 3). The orientation of the first frame is such that you are watching from the inside of the circuit towards the outside through the funnel opening. The epicard of the atria is at the top of the view, and the endocardial side of the atrial wall is at the bottom.

Video V8: 3D Trapping: Three-dimensional trapping and releasing of an excitation wave in the full atria corresponding to the process in Figure 6. A rotation of the atria is shown in the movie as well, to familiarize oneself with the atrial geometry. The movie has been slowed down 10 times with respect to

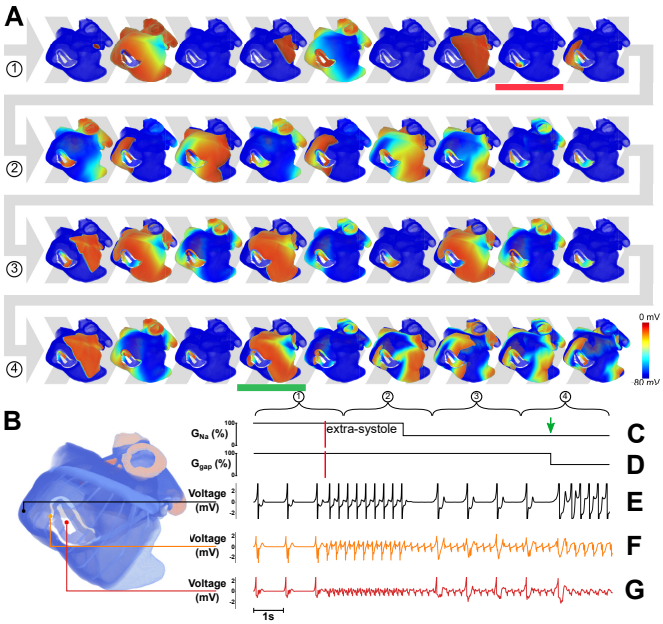

Figure S6 – **Alternative schematic circuit designs to create trapped reentry.** A, Visualization of the steps involved in trapped reentry through representative voltage maps (3 pictures/second, 12 seconds in total). The horizontal red bar denotes the moment an extrasystole occurs, while the horizontal green bar marks the escape of the trapped excitation wave. Trapping occurs when the sodium conductance decreases. B, Enlargement of the human atria with different anatomical regions indicated by different colors. C, Relative sodium conductance. D, Relative gap junctional coupling efficiency. E, Unipolar electrogram from the bulk atrial tissue showing alternating slow and fast pacing frequencies corresponding to SR and reentrant driver frequencies. F-G, Unipolar electrograms next to the circuit of trapped reentry showing fractionation during SR.

real-time (timer indicates real-time seconds) to see the effect of trapping and releasing of the excitation waves clearly.

Video V9: 3D Unipolar Electrograms Protocol 1: Realtime visualization (timer indicates seconds) of trapped reentry voltage maps together with 3 unipolar electrograms. The 12 second protocol of Figure 6 is shown in a movie that takes exactly those same 12 seconds to run.

References

[1] Ayodele Odutayo, Christopher X Wong, Allan J Hsiao, Sally Hopewell, Douglas G Altman, and Connor A Emdin. Atrial fibrillation and risks of cardiovascular disease, renal disease, and death: systematic review and meta-analysis. *bmj*, 354, 2016.

[2] A John Camm, Osmar Antonio Centurión, Shojiro Isomoto, Akihiko Shimizu, Atsushi Konoe, Muneshige

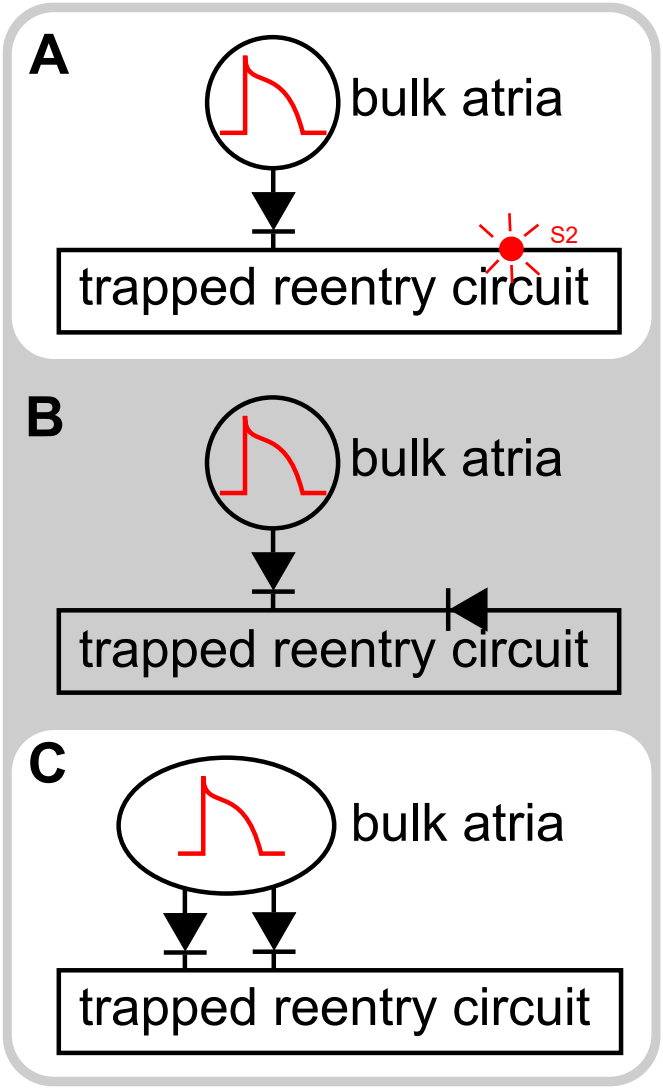

Figure S7 – **Alternative schematic circuit designs to create trapped reentry.** An analogy was made with an electrical circuit, where the SA node and bulk is depicted by a circle with a simplified action potential, and the entrance to the circuit is denoted by a diode, signifying unidirectional block A) The design that was used in the main manuscript, making use of an S2-pulse to create reentry B) A design making use of two unidirectional blocks to create reentry. C) A design making use of two unidirectional entrances that can start reentry.

Kaibara, Tetsuya Hirata, Osamu Hano, Ryoji Sakamoto, Motonobu Hayano, et al. The effects of aging on atrial endocardial electrograms

Circuit	Long			Short		
Model	CRN	CRN AF	Loewe	CRN	CRN AF	Loewe
	Enter					
G_{Na}-min (%)	31.4	32.1	34.8	31.4	32.1	34.8
G_{Na}-max (%)	100.0	100.0	100.0	100.0	100.0	100.0
	Block					
G_{Na}-S2 (%)	80.0	100.0	100.0	N/A	80.0	100.0
G_{Na}-min (%)	30.6	29.5	32.5	N/A	37.4	32.7
G_{Na}-max (%)	41.3	42.3	45.5	N/A	42.4	45.5
	Release					
G_{Na}-min (%)	37.0	39.0	43.0	N/A	39.0	44.0
G_{Na}-max (%)	41.3	42.3	45.5	N/A	42.4	45.5
D-min (%)	20.0	10.0	30.0	N/A	10.0	30.0
D-max (%)	90.0	90.0	90.0	N/A	90.0	90.0

Table. S8 – **Parameters for both circuits of trapped re-entry for all three human atrial models.** Three different scenarios are depicted, the one of entering the circuit, getting trapped in the circuit and release of excitation waves from the circuit. CRN: Courtemanche model, CRN AF: Courtemanche AF model

in patients with paroxysmal atrial fibrillation. *Clinical Cardiology: An International Indexed and Peer-Reviewed Journal for Advances in the Treatment of Cardiovascular Disease*, 26(9):435–438, 2003.

[3] Madison S Spach, J Francis Heidlage, Paul C Dolber, and Roger C Barr. Mechanism of origin of conduction disturbances in aging human atrial bundles: experimental and model study. *Heart rhythm*, 4(2):175–185, 2007.

[4] Madison S Spach and Paul C Dolber. Relating extracellular potentials and their derivatives to anisotropic propagation at a microscopic level in human cardiac muscle. evidence for electrical uncoupling of side-to-side fiber connections with increasing age. *Circulation research*, 58(3):356–371, 1986.

[5] Madison S Spach and John P Boineau. Microfibrosis produces electrical load variations due to loss of side-to-side cell connections; a major mechanism of structural heart disease arrhythmias. *Pacing and clinical electrophysiology*, 20(2):397–413, 1997.

[6] Michel Haissaguerre, Pierre Jaïs, Dipen C Shah, Atsushi Takahashi, Mélèze Hocini, Gilles Quiniou, Stéphane Garrigue, Alain Le Mouroux, Philippe Le Métayer, and Jacques Clémenty. Spontaneous initiation of atrial fibrillation by ectopic beats originating in the pulmonary veins. *New England Journal of Medicine*, 339(10):659–666, 1998.

[7] Maurits A Allessie, FI Bonke, and FJ Schopman. Circus movement in rabbit atrial muscle as a mechanism of tachycardia. ii. the role of nonuniform recovery of excitability in the occurrence of unidirectional block, as studied with multiple microelectrodes. *Circulation research*, 39(2):168–177, 1976.

[8] Hans Kottkamp. Human atrial fibrillation substrate: towards a specific fibrotic atrial cardiomyopathy. *European heart journal*, 34(35):2731–2738, 2013.

[9] Brian J Hansen, Jichao Zhao, Thomas A Csepe, Brandon T Moore, Ning Li, Laura A Jayne, Anuradha Kalyanasundaram, Praise Lim, Anna Bratasz, Kimerly A Powell, et al. Atrial fibrillation driven

by micro-anatomic intramural re-entry revealed by simultaneous sub-epicardial and sub-endocardial optical mapping in explanted human hearts. *European heart journal*, 36(35):2390–2401, 2015.

[10] Atul Verma, Chen-yang Jiang, Timothy R Betts, Jian Chen, Isabel Deisenhofer, Roberto Mantovan, Laurent Macle, Carlos A Morillo, Wilhelm Haverkamp, Rukshen Weerasooriya, et al. Approaches to catheter ablation for persistent atrial fibrillation. *New England Journal of Medicine*, 372(19):1812–1822, 2015.

[11] Jose C Pachon M, Enrique I Pachon M, Juan C Pachon M, Tasso J Lobo, Maria Z Pachon, Remy NA Vargas, Denilda QV Pachon, Francisco J Lopez M, and Adib D Jatene. A new treatment for atrial fibrillation based on spectral analysis to guide the catheter rf-ablation. *EP Europace*, 6(6):590–601, 2004.

[12] Mauricio Arruda and Andrea Natale. Ablation of permanent af: adjunctive strategies to pulmonary veins isolation: targeting af nest in sinus rhythm and cfae in af. *Journal of interventional cardiac electrophysiology*, 23:51–57, 2008.

[13] Sanjiv M Narayan, David E Krummen, Kalyanam Shivkumar, Paul Clopton, Wouter-Jan Rappel, and John M Miller. Treatment of atrial fibrillation by the ablation of localized sources: Confirm (conventional ablation for atrial fibrillation with or without focal impulse and rotor modulation) trial. *Journal of the American College of Cardiology*, 60(7):628–636, 2012.

[14] Koonlawee Nademanee, John McKenzie, Erol Kosar, Mark Schwab, Buncha Sunsaneewitayakul, Thaveekiat Vasavakul, Chotikorn Khunnawat, and Tachapong Ngarmukos. A new approach for catheter ablation of atrial fibrillation: mapping of the electrophysiologic substrate. *Journal of the American College of Cardiology*, 43(11):2044–2053, 2004.

[15] Jiaxiong Lin, Benjamin J Scherlag, Jing Zhou, Zhibing Lu, Eugene Patterson, Warren M Jackman, Ralph Lazzara, and Sunny S Po. Autonomic mechanism to explain complex fractionated atrial electrograms (cfae). *Journal of cardiovascular electrophysiology*, 18(11):1197–1205, 2007.

[16] Karen TS Konings, Joep LRM Smeets, Olaf C Penn, Hein JJ Wellens, and Maurits A Allessie. Configuration of unipolar atrial electrograms during electrically induced atrial fibrillation in humans. *Circulation*, 95(5):1231–1241, 1997.

[17] Sonja Kleinlogel, Katrin Feldbauer, Robert E Dempski, Heike Fotis, Phillip G Wood, Christian Bamann, and Ernst Bamberg. Ultra light-sensitive and fast neuronal activation with the ca2+-permeable channelrhodopsin catch. *Nature neuroscience*, 14(4):513–518, 2011.

[18] Iolanda Feola, Linda Volkers, Rupamanjari Majumder, Alexander Teplenin, Martin J. Schalij, Alexander V. Panfilov, Antoine A.F. de Vries, and Daniël A. Pijnappels. Localized optogenetic targeting of rotors in atrial cardiomyocyte monolayers. *Circulation: Arrhythmia and Electrophysiology*, 10(11):e005591, 2017.

[19] Candido Cabo, Arkady M Pertsov, William T Baxter, Jorge M Davidenko, Richard A Gray, and Jose Jalife. Wave-front curvature as a cause of slow conduction and block in isolated cardiac muscle. *Circulation research*, 75(6):1014–1028, 1994.

[20] Stephan Rohr, Jan P Kucera, Vladimir G Fast, and André G Kléber. Paradoxical improvement of impulse conduction in cardiac tissue by partial cellular uncoupling. *Science*, 275(5301):841–844, 1997.

[21] Iolanda Feola, Alexander Teplenin, Antoine AF de Vries, and Daniël A Pijnappels. Optogenetic engineering of atrial cardiomyocytes. *Optogenetics: Methods and Protocols*, pages 319–331, 2016.

[22] Rupamanjari Majumder, Wanchana Jangsangthong, Iolanda Feola, Dirk L Ypey, Daniël A Pijnappels, and Alexander V Panfilov. A mathematical model of neonatal rat atrial monolayers with constitutively active acetylcholine-mediated k+ current. *PLoS computational biology*, 12(6):e1004946, 2016.

[23] John C. Williams, Jianjin Xu, Zhongju Lu, Aleksandra Klimas, Xuxin Chen, Christina M. Ambrosi, Ira S. Cohen, and Emilia Entcheva. Computational optogenetics: Empirically-derived voltage- and light-sensitive channelrhodopsin-2 model. *PLOS Computational Biology*, 9(9):1–19, 09 2013.

[24] Olaf Dössel, Martin W Krueger, Frank M Weber, Christopher Schilling, Walther HW Schulze, and Gunnar Seemann. A framework for personalization of computational models of the human atria. In *2011 Annual International Conference of the IEEE Engineering in Medicine and Biology Society*, pages 4324–4328. IEEE, 2011.

[25] Marc Courtemanche, Rafael J Ramirez, and Stanley Nattel. Ionic mechanisms underlying human atrial action potential properties: insights from a mathematical model. *American Journal of Physiology-Heart and Circulatory Physiology*, 275(1):H301–H321, 1998.

[26] Marc Courtemanche, Rafael J Ramirez, and Stanley Nattel. Ionic targets for drug therapy and atrial fibrillation-induced electrical remodeling: insights from a mathematical model. *Cardiovascular research*, 42(2):477–489, 1999.

[27] Axel Loewe, Yannick Lutz, Mathias Wilhelms, Daniel Sinnecker, Petra Barthel, Eberhard P Scholz, Olaf Dössel, Georg Schmidt, and Gunnar Seemann. In-silico assessment of the dynamic effects of amiodarone and dronedarone on human atrial patho-electrophysiology. *Europace*, 16(suppl_4):iv30–iv38, 2014.

[28] Jeffrey L Anderson, Benjamin D Horne, and Dudley J Pennell. Atrial dimensions in health and left ventricular disease using cardiovascular magnetic resonance. *Journal of Cardiovascular Magnetic Resonance*, 7(4):671–675, 2005.

[29] Vincent Jacquemet, Nathalie Virag, Zenichi Ihara, LAM Dang, Olivier Blanc, Steeve Zozor, JEAN-MARC VESIN, Lukas Kappenberger, and Craig Henriquez. Study of unipolar electrogram morphology in a computer model of atrial fibrillation. *Journal of cardiovascular electrophysiology*, 14:S172–S179, 2003.

[30] Vladimir G Fast and Andre G Kleber. Block of impulse propagation at an abrupt tissue expansion: evaluation of the critical strand diameter in 2-and 3-dimensional computer models. *Cardiovascular research*, 30(3):449–459, 1995.

[31] Peter Spector. Principles of cardiac electric propagation and their implications for re-entrant arrhythmias. *Circulation: Arrhythmia and Electrophysiology*, 6(3):655–661, 2013.

[32] Vladimir G Fast and André G Kléber. Cardiac tissue geometry as a determinant of unidirectional conduction block: assessment of microscopic excitation spread by optical mapping in patterned cell cultures and in a computer model. *Cardiovascular research*, 29(5):697–707, 1995.

[33] T Alexander Quinn, Patrizia Camelliti, Eva A Rog-Zielinska, Urszula Siedlecka, Tommaso Poggioli, Eileen T O'Toole, Thomas Knopfel, and Peter Kohl. Electrotonic coupling of excitable and nonexcitable cells in the heart revealed by optogenetics. *Proceedings of the National Academy of Sciences*, 113(51):14852–14857, 2016.

[34] Michele Miragoli, Nicolo Salvarani, and Stephan Rohr. Myofibroblasts induce ectopic activity in cardiac tissue. *Circulation research*, 101(8):755–758, 2007.

[35] Stefan Dhein, Thomas Seidel, Aida Salameh, Joanna Jozwiak, Anja Hagen, Martin Kostelka, Gerd Hindricks, and Friedrich-Wilhelm Mohr. Remodeling of cardiac passive electrical properties and susceptibility to ventricular and atrial arrhythmias. *Frontiers in Physiology*, 5:424, 2014.

[36] Robin M Shaw and Yoram Rudy. Electrophysiologic effects of acute myocardial ischemia: a theoretical study of altered cell excitability and action potential duration. *Cardiovascular research*, 35(2):256–272, 1997.

[37] A Müller and S Dhein. Sodium channel blockade enhances dispersion of the cardiac action potential duration: a computer simulation study. *Basic research in cardiology*, 88:11–22, 1993.

[38] Carol Ann Remme and Connie R Bezzina. Sodium channel (dys) function and cardiac arrhythmias. *Cardiovascular therapeutics*, 28(5):287–294, 2010.

[39] S Dhein and S-B Hammerath. Aspects of the intercellular communication in aged hearts: effects of the gap junction uncoupler palmitoleic acid. *Naunyn-Schmiedeberg's archives of pharmacology*, 364(5), 2001.

[40] Sergio Alonso, Rodrigo Weber Dos Santos, and Markus Bär. Reentry and ectopic pacemakers emerge in a three-dimensional model for a slab of cardiac tissue with diffuse microfibrosis near the percolation threshold. *PloS one*, 11(11):e0166972, 2016.

[41] Rafael Sachetto Oliveira, Sergio Alonso, Fernando Otaviano Campos, Bernardo Martins Rocha, João Filipe Fernandes, Titus Kuehne, and Rodrigo Weber Dos Santos. Ectopic beats arise from micro-reentries near infarct regions in simulations of a patient-specific heart model. *Scientific reports*, 8(1):1–14, 2018.

[42] Qing Lou, Brian J Hansen, Olga Fedorenko, Thomas A Csepe, Anuradha Kalyanasundaram, Ning Li, Lori T Hage, Alexey V Glukhov, George E Billman, Raul Weiss, et al. Upregulation of adenosine a1 receptors facilitates sinoatrial node dysfunction in chronic canine heart failure by exacerbating nodal conduction abnormalities revealed by novel dual-sided intramural optical mapping. *Circulation*, 130(4):315–324, 2014.

[43] Ning Li, Anuradha Kalyanasundaram, Brian J Hansen, Esthela J Artiga, Roshan Sharma, Suhaib H Abudulwahed, Katelynn M Helfrich, Galina Rozenberg, Pei-Jung Wu, Stanislav Zakharkin, et al.

Impaired neuronal sodium channels cause intranodal conduction failure and reentrant arrhythmias in human sinoatrial node. *Nature communications*, 11(1):512, 2020.

[44] Buyun Xu, Chao Xu, Yong Sun, Jiahao Peng, Fang Peng, Weiliang Tang, Yan Zhou, Shengkai Wang, Jie Pan, and Yangbo Xing. Fixed complex electrograms during sinus rhythm and local pacing: potential ablation targets for persistent atrial fibrillation. *Scientific Reports*, 12(1):10697, 2022.

[45] YENN-JIANG LIN, SHIH-LIN CHANG, LI-WEI LO, YU-FENG HU, Kazuyoshi Suenari, CHENG-HUNG LI, TZE-FAN CHAO, FA-PO CHUNG, JO-NAN LIAO, Beny Hartono, et al. A prospective, randomized comparison of modified pulmonary vein isolation versus conventional pulmonary vein isolation in patients with paroxysmal atrial fibrillation. *Journal of cardiovascular electrophysiology*, 23(11):1155–1162, 2012.

[46] Seil Oh, HYOUN-JOONG KONG, EUE-KEUN CHOI, Hee Chan Kim, and YUN-SHIK CHOI. Complex fractionated electrograms and af nests in vagally mediated atrial fibrillation. *Pacing and clinical electrophysiology*, 33(12):1497–1503, 2010.

[47] Eduardo Franco, Cristina Lozano Granero, Nuno Cortez-Dias, Elad Nakar, Meytal Segev, Roberto Matía, Antonio Hernández-Madrid, José Luis Zamorano, and Javier Moreno. Automatic identification of areas with low-voltage fragmented electrograms for the detection of the critical isthmus of atypical atrial flutters. *Journal of Cardiovascular Electrophysiology*, 34(2):356–365, 2023.

[48] Stuart P Thomas, Elisabeth M Wallace BSc, and David L Ross. The effect of a residual isthmus of surviving tissue on conduction after linear ablation in atrial myocardium. *Journal of Interventional Cardiac Electrophysiology*, 4:273–281, 2000.

[49] Arkady M Pertsov, Jorge M Davidenko, Remy Salomonsz, William T Baxter, and Jose Jalife. Spiral waves of excitation underlie reentrant activity in isolated cardiac muscle. *Circulation research*, 72(3):631–650, 1993.

[50] Stanley Rush and Hugh Larsen. A practical algorithm for solving dynamic membrane equations. *IEEE Transactions on Biomedical Engineering*, (4):389–392, 1978.

[51] FRACP Stuart P Thomas BMed, Elisabeth M Wallace BSc, and FRACP David L Ross MB BS. *Journal of Interventional Cardiac Electrophysiology*, 4(1):273–281, 2000.

[52] Hugh Calkins, Gerhard Hindricks, Riccardo Cappato, Young-Hoon Kim, Eduardo B Saad, Luis Aguinaga, Joseph G Akar, Vinay Badhwar, Josep Brugada, John Camm, Peng-Sheng Chen, Shih-Ann Chen, Mina K Chung, Jens Cosedis Nielsen, Anne B Curtis, D Wyn Davies, John D Day, André d'Avila, N M S (Natasja) de Groot, Luigi Di Biase, Mattias Duytschaever, James R Edgerton, Kenneth A Ellenbogen, Patrick T Ellinor, Sabine Ernst, Guilherme Fenelon, Edward P Gerstenfeld, David E Haines, Michel Haissaguerre, Robert H Helm, Elaine Hylek, Warren M Jackman, Jose Jalife, Jonathan M Kalman, Josef Kautzner, Hans Kottkamp, Karl Heinz Kuck, Koichiro Kumagai, Richard Lee, Thorsten Lewalter, Bruce D Lindsay, Laurent Macle, Moussa Mansour, Francis E

Marchlinski, Gregory F Michaud, Hiroshi Nakagawa, Andrea Natale, Stanley Nattel, Ken Okumura, Douglas Packer, Evgeny Pokushalov, Matthew R Reynolds, Prashanthan Sanders, Mauricio Scanavacca, Richard Schilling, Claudio Tondo, Hsuan-Ming Tsao, Atul Verma, David J Wilber, Teiichi Yamane, Carina Blomström-Lundqvist, Angelo A V De Paola, Peter M Kistler, Gregory Y H Lip, Nicholas S Peters, Cristiano F Pisani, Antonio Raviele, Eduardo B Saad, Kazuhiro Satomi, Martin K Stiles, and Stephan Willems and. 2017 HRS/EHRA/ECAS/APHRS/SOLAECE expert consensus statement on catheter and surgical ablation of atrial fibrillation. *EP Europace*, 20(1):e1–e160, September 2017.

[53] Stanley Rush and Hugh Larsen. A practical algorithm for solving dynamic membrane equations. *IEEE Transactions on Biomedical Engineering*, BME-25(4):389–392, July 1978.

[54] P. Comtois, J. Kneller, and S. Nattel. Of circles and spirals: Bridging the gap between the leading circle and spiral wave concepts of cardiac reentry. *EP Europace*, 7(s2):S10–S20, January 2005.

[55] MS Spach, PC Dolber, and JF Heidlage. Influence of the passive anisotropic properties on directional differences in propagation following modification of the sodium conductance in human atrial muscle. a model of reentry based on anisotropic discontinuous propagation. *Circulation research*, 62(4):811–832, 1988.

[56] Yoshihiko Nagai, Hortensia González, Alvin Shrier, and Leon Glass. Paroxysmal starting and stopping of circulating waves in excitable media. *Physical review letters*, 84(18):4248, 2000.